ATLAS CONF Note

ATLAS-CONF-2022-057

9th September 2022

Search for direct production of winos and higgsinos in events with two same-sign or three leptons in pp collision data at $\sqrt{s} = 13$ TeV with the ATLAS detector

The ATLAS Collaboration

A search for supersymmetry targeting the direct production of winos and higgsinos is conducted in final states with either two leptons (e or μ) with the same electric charge, or at least three leptons. The analysis uses 139 fb^{-1} of pp collision data at $\sqrt{s} = 13$ TeV collected with the ATLAS detector during Run 2 of the Large Hadron Collider. No significant excess over the Standard Model expectation is observed. Simplified and complete models with and without R-parity conservation are considered. In topologies with intermediate states including either Wh or WZ pairs, wino masses up to 525 GeV and 260 GeV are excluded, respectively, for a bino of vanishing mass. Higgsino masses smaller than 440 GeV are excluded in a natural R-parity-violating model with bilinear terms. Upper limits on the production cross section of generic events beyond the Standard Model as low as 40 ab are obtained in signal regions optimised for these models and also for an R-parity violating scenario with baryon-number-violating higgsino decays to top quarks and jets.

ATLAS-CONF-2022-057
09 September 2022

1 Introduction

Experimental searches for signals of physics beyond the Standard Model (SM) at colliders have long exploited the signature of final states with a pair of isolated light leptons (electrons or muons) with the same-sign (SS) electric charge. In the SM, the production of such lepton pairs is rare and originates mainly from weak-boson decays. In proton-proton (pp) collisions at $\sqrt{s}$ = 13 TeV, the inclusive cross section is of the order of one pb [1, 2], hence it is suppressed by more than three orders of magnitude relative to the production of opposite-sign lepton pairs. On the other hand, heavy particles beyond the SM (BSM) could decay into multiple massive SM bosons or top quarks, which subsequently decay with considerable branching ratios into same-sign leptons and jets. Examples of such BSM states include supersymmetric (SUSY) particles [3, 4], SS top-quark pairs [5, 6], scalar gluons (sgluons) [7, 8], heavy scalar bosons of extended Higgs sectors [9, 10], Majorana heavy neutrinos [11, 12], and vector-like top quarks [13].

At the Large Hadron Collider (LHC) [14], the ATLAS [15] and CMS [16] experiments have extensively probed possible SM extensions in the same-sign dilepton channel. Among these theoretical proposals, SUSY [17–23] remains a compelling framework as it provides solutions to the gauge hierarchy problem [24–27] without the need for large fine tuning of fundamental parameters [28, 29], offers gauge coupling unification [24–27], and contains weakly interacting particles that can contribute to the dark matter [30, 31].

Charginos, $\tilde{\chi}^{\pm}_{1,2}$, and neutralinos, $\tilde{\chi}^{0}_{1,2,3,4}$, collectively referred to as 'electroweakinos', are the ordered mass eigenstates formed from the linear superposition of the higgsinos, winos, and binos, which are the SUSY partners of the Higgs and electroweak gauge bosons, respectively. A discrete multiplicative symmetry, R-parity [32], is often introduced in SUSY models to avoid rapid proton decay. If R-parity is conserved (RPC) the lightest supersymmetric particle (LSP) is stable and is required to be neutral and colourless to evade observation [33]. Therefore, it would be invisible in a hadron collider experiment, only manifested through large missing transverse momentum, $E_{\mathrm{T}}^{\mathrm{miss}}$. There is no fundamental theoretical reason to impose R-parity conservation, and R-parity-violating (RPV) SUSY models [34] are also well motivated, while introducing more parameters to constrain. In RPV SUSY, a $\tilde{\chi}^{0}_{1}$ LSP would decay to SM particles and, due to its Majorana nature, it may give rise to SS lepton final states.

In this article, the search described in Ref. [35] is extended to more signal models using the full data set of pp collisions at $\sqrt{s}$ = 13 TeV recorded by the ATLAS detector during the LHC Run 2, corresponding to an integrated luminosity of 139 fb^{-1}. The selection is based on final states with two SS leptons or three leptons accompanied by large $E_{\mathrm{T}}^{\mathrm{miss}}$ and a number of hadronic jets, possibly tagged as b-jets. This search represents the first ATLAS result from a two-SS-lepton selection targeting direct chargino and neutralino production. Such production may be dominant at the LHC according to naturalness considerations [28, 29], which suggest that the lightest electroweakinos have masses near the electroweak scale while the superpartners of the gluon and quarks can be heavier than a few TeV. This search covers so-far unconstrained kinematic regions, not yet excluded by previous three lepton analyses. The smaller background faced by SS-lepton analyses allows to impose looser kinematic requirements, e.g. on $E_{\mathrm{T}}^{\mathrm{miss}}$ or on the momenta of jets and leptons, which provides sensitivity to scenarios with small mass splittings between the superpartners [36–38] or RPV models. In addition to exploring directly such scenarios, the analysis provides signal regions orthogonal to others targeting different final states, thus improving the overall sensitivity through future statistical combinations. The event selection provides optimal sensitivity to four target models: (i, ii) simplified models of winos and binos with on-shell WZ or Wh as intermediate states; (iii) higgsino production with bilinear R-parity-violating (bRPV) terms; and (iv) higgsino production with R-parity violating decays to top quarks via baryon-number violating UDD couplings.

All prior searches for SS lepton pairs and several three-lepton searches carried out by ATLAS [35, 39–43] and CMS [44–46] focused on strong production of superpartners, on electroweak SUSY production with low hadronic activity, or on slepton resonant production [47]. Other analyses with three-lepton selections focused on direct electroweakino production in events without jets [48–56] or in trilepton resonances [57].

Simplified models with $\tilde{\chi}_1^{\pm}\tilde{\chi}_2^0$ production and Wh bosons in the decay chain have been explored by ATLAS in fully hadronic [58], semileptonic [40], photon [59], and multilepton [43] final states with large $E_{\mathrm{T}}^{\mathrm{miss}}$. CMS has constrained this scenario by combining a variety of leptonic signatures, including SS dileptons and τ-leptons [46, 60]. Intermediate decays to WZ bosons have been probed previously in ATLAS assuming boosted hadronically decaying bosons [58] and three leptons [56] in the final state. CMS has investigated this channel in a searches for multileptons [60], for SS or three leptons [46], and soft leptons [38].

ATLAS has set limits on bRPV models assuming strong superpartner production [61]. Minimal Supergravity [62–64] with bilinear terms has been constrained in events with one lepton [65, 66], one τ [67], or two SS leptons [39], and in their combination [68]. A reinterpretation of a SS lepton analysis [39] set bounds [69] in a 'natural' bRPV scenario [28, 29] within the phenomenological Minimal Supersymmetric Standard Model (pMSSM) [70, 71].

Baryonic UDD operators have been probed by the ATLAS [58, 72–77] and CMS [45, 78–82] experiments in multijet final states and by ATLAS in events with at least one lepton [83]. Models with $\tilde{\chi}_1^0 \to tbs$ have been constrained in gluino and top squark production in a wide range of λ''_{323} couplings, by reinterpreting several ATLAS searches optimised for RPC and RPV SUSY models [84].

The paper is structured as follows. Section 2 is dedicated to the targeted signal models. Details of the ATLAS detector are described in Section 3, with the utilised data set and simulation samples listed in Section 4. The object definitions and the event categorisation are discussed in Section 5 and Section 6, respectively. The background modelling and validation is given in Section 7. Systematic uncertainties are discussed in Section 8, and the results and interpretations are presented in Section 9 and Section 10, respectively. The conclusions are summarised in Section 11. Finally, details of the UDD RPV model analysis are discussed in Appendix A.

2 Signal models

The models targeted in this analysis can be divided into two main scenarios: directly produced wino-like electroweakinos with bino-like LSP in RPC SUSY, shown in Figure 1, and higgsino-like electroweakinos with RPV terms, depicted in Figure 2.

2.1 Wino-bino $\tilde{\chi}_1^{\pm}\tilde{\chi}_2^0$ production with Wh or WZ bosons

Simplified models [85–87] involving the direct production of a lightest chargino, $\tilde{\chi}_1^{\pm}$, and a next-to-lightest neutralino, $\tilde{\chi}_2^0$ are considered. The $\tilde{\chi}_1^{\pm}$ and the $\tilde{\chi}_2^0$ are assumed to be mass-degenerate and wino-like, i.e. superpartners of the $SU(2)_L$ gauge fields, whilst the $\tilde{\chi}_1^0$ is bino-like, i.e. superpartner of the $U(1)_Y$ gauge field [2]. The $\tilde{\chi}_1^{\pm}$ is assumed to decay to an on-shell, leptonically decaying W and $\tilde{\chi}_1^0$, while for the $\tilde{\chi}_2^0$ two decay cases are examined: (i) A Higgs boson featuring SM-Higgs properties is considered, which is the dominant decay for many choices of MSSM parameters as long as the mass-splitting between the two lightest neutralinos is larger than the Higgs boson mass and the higgsinos are heavier than the winos.

All possible decays of the Higgs boson which ultimately result in a single lepton and jets (mostly via intermediate states) are taken into account. This is indicated by the grey-filled dot in the Higgs decay in Figure 1(a). (ii) A decay into an on-shell, leptonically decaying Z is also studied, as shown in Figure 1(b).

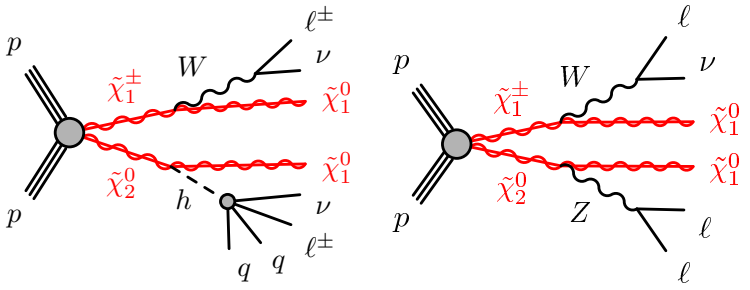

(a) Wino $\tilde{\chi}_1^\pm\tilde{\chi}_2^0$ with Wh (b) Wino $\tilde{\chi}_1^\pm\tilde{\chi}_2^0$ with WZ

Figure 1: Diagrams of the targeted RPC simplified models with intermediate gauge vector and Higgs boson production.

2.2 Higgsino-like electroweakinos in RPV scenarios

The RPV component of the generic superpotential can be written as [34]:

$$W_{\not R_p} = \frac{1}{2}\lambda_{ijk}L_iL_j\bar{E}_k + \lambda'_{ijk}L_iQ_j\bar{D}_k + \epsilon_iL_iH_2 + \frac{1}{2}\lambda''_{ijk}\bar{U}_i\bar{D}_j\bar{D}_k, \tag{1}$$

where $i, j, k = 1, 2, 3$ are generation indices. The L_i, Q_i represent the lepton and quark $SU(2)_L$ doublet superfields, whereas H_2 is the Higgs superfield. The $\bar{E}_j$, $\bar{D}_j$, and $\bar{U}_j$ are the charged lepton, down-type quark, and up-type quark $SU(2)_L$ singlet superfields, respectively. The Yukawa couplings are λ, λ', and λ'', whilst ϵ is a dimensionful mass parameter. We explore two RPV scenarios, the first from bilinear lepton-number-violating terms LH_2, and the second from baryon-number violating terms UDD in Eq. (1).

RPV SUSY through bilinear terms is strongly motivated by its inherent connection with neutrino physics [88–90]. Sneutrino vacuum expectation values (VEVs) introduce a mixing between neutrinos and neutralinos, leading to a see-saw mechanism that gives mass to one neutrino at tree level with the other two neutrino masses being induced by loop effects [91, 92]. The same VEVs are also involved in the decay of the LSP, thus constraining it by experimental neutrino measurements.

The specific model considered here is inspired by naturalness [28, 29] arguments and involves the pair production of light, nearly degenerate higgsinos, $\tilde{\chi}_2^0$, $\tilde{\chi}_1^\pm$ and $\tilde{\chi}_1^0$, with mass splittings below 2 GeV [93]. The dominant production processes are $\tilde{\chi}_1^\pm\tilde{\chi}_1^0$, $\tilde{\chi}_1^\pm\tilde{\chi}_2^0$, $\tilde{\chi}_1^0\tilde{\chi}_2^0$, and $\tilde{\chi}_1^\pm\tilde{\chi}_1^\mp$, among which only the first three feature a two-SS-lepton final state. A low ratio of Higgs doublets VEVs, $\tan\beta = 5$, is assumed to favour higgsino decays to light leptons at the expense of decays to τ-leptons, prefered by more than 90% at high $\tan\beta$. Dominant decays include $\tilde{\chi}_1^\pm \to W^\pm\nu_\mu$, $\tilde{\chi}_{1,2}^0 \to W^\pm\ell^\mp, W^\pm\tau^\mp$, and $\tilde{\chi}_2^0 \to \tilde{\chi}_1^\pm\pi^\mp$, hence SS dilepton and trilepton final states occur from W and τ leptonic decays. Examples of diagrams are given in Figure 2(a) and Figure 2(b). The decay modes are partly determined by a fit to neutrino oscillation experimental data [94], leading to flavour non-universality of lepton decays, with more details given in Section 4. All possible allowed higgsino decays are considered in the analysis.

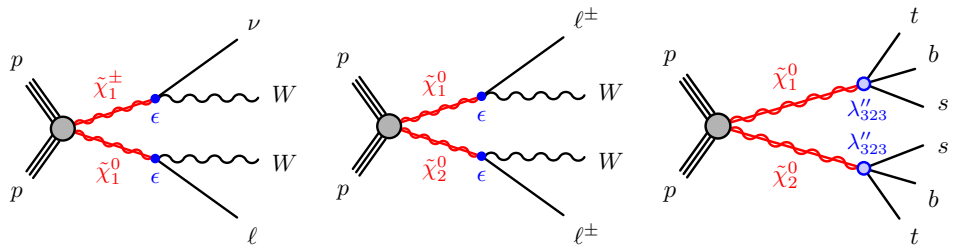

(a) Higgsino $\tilde{\chi}_1^{\pm}\tilde{\chi}_1^0$ bRPV (b) Higgsino $\tilde{\chi}_1^0\tilde{\chi}_2^0$ bRPV (c) Higgsino $\tilde{\chi}_1^0\tilde{\chi}_2^0$ *UDD* RPV

Figure 2: Diagrams of the targeted RPV models. Diagrams (a) and (b) serve as examples, as inclusive bRPV production is considered. The *UDD* RPV scenario with BNV terms in diagram (c) is a simplified model.

Besides SUSY with *UDD* terms in Eq. (1) [34, 95, 96], baryon number violation (BNV) is featured in BSM scenarios such as grand unified theories [97] and models with black holes [98]. Moreover, BNV is fundamental to explain the observed asymmetry between baryons and antibaryons in the universe as an evolution from an early symmetric state [99].

In the simplified topology considered, higgsino $\tilde{\chi}_1^0\tilde{\chi}_2^0$ pairs are directly produced and undergo prompt RPV decays as shown in the diagram of Figure 2(c). The UDD-type BNV coupling λ''_{323}, defined in Eq. (1), is chosen to be non-vanishing, as it is predicted to be dominant under the minimal flavour violation hypothesis [96]. Its value is chosen to be $O(10^{-3})$ to $O(10^{-2})$, which guarantees prompt decays for electroweakino masses down to 180 GeV. The $\tilde{\chi}_2^0$ NLSP and the $\tilde{\chi}_1^0$ LSP are mass degenerate and decay with a 100% branching ratio to tbs, thus possibly leading to a final state with two SS leptons and at least six jets of which at least four b-jets. Other electroweakino production modes do not lead to the final states targeted by this search.

3 ATLAS detector

The ATLAS detector [15] is a multipurpose particle detector with a forward–backward symmetric cylindrical geometry and a near 4π coverage in solid angle.[1] It consists of an inner tracking detector surrounded by a thin superconducting solenoid providing a 2 T axial magnetic field, electromagnetic and hadronic calorimeters, and a muon spectrometer. The inner tracking detector (ID) covers the pseudorapidity range $|\eta| < 2.5$. It consists of silicon pixel, silicon microstrip, and transition radiation tracking detectors. An additional layer of silicon pixels, the insertable B-layer [100, 101], was installed before Run 2. Lead/liquid-argon (LAr) sampling calorimeters provide electromagnetic (EM) energy measurements with high granularity. A steel/scintillator-tile hadron calorimeter covers the central pseudorapidity range ($|\eta| < 1.7$). The endcap and forward regions are instrumented with LAr calorimeters for both the EM and hadronic energy measurements up to $|\eta| = 4.9$. The muon spectrometer surrounds the calorimeters and is based on three large superconducting air-core toroidal magnets with eight coils each. The field integral of the toroids ranges between 2.0 and 6.0 T m across most of the detector. The muon spectrometer (MS) includes a

[1] ATLAS uses a right-handed coordinate system with its origin at the nominal interaction point (IP) in the centre of the detector and the z-axis along the beam pipe. The x-axis points from the IP to the centre of the LHC ring, and the y-axis points upwards. Cylindrical coordinates (r, ϕ) are used in the transverse plane, ϕ being the azimuthal angle around the z-axis. The pseudorapidity is defined in terms of the polar angle θ as $\eta = -\ln\tan(\theta/2)$. Angular distance is measured in units of $\Delta R \equiv \sqrt{(\Delta\eta)^2 + (\Delta\phi)^2}$.

system of precision chambers for tracking and fast detectors for triggering. A two-level trigger system is used to select events. The first-level trigger is implemented in hardware and uses a subset of the detector information to accept events at a rate below 100 kHz. This is followed by a software-based trigger that reduces the accepted event rate to 1 kHz on average depending on the data-taking conditions. An extensive software suite [102] is used in the reconstruction and analysis of real and simulated data, in detector operations, and in the trigger and data acquisition systems of the experiment.

4 Data set and simulated event samples

This paper analyses proton–proton collision data collected by the ATLAS detector between 2015 and 2018. In this period, the LHC delivered colliding beams with a peak instantaneous luminosity up to $2.1 \times 10^{34}\,\text{cm}^{-2}\,\text{s}^{-1}$, achieved in 2018, and an average number of pp interactions per bunch crossing, $\langle\mu\rangle$, of 33.7. After the application of beam, detector, and data-quality criteria [103], the total integrated luminosity of the dataset was 139 fb^{-1} with a combined uncertainty of 1.7% [104], obtained using the LUCID-2 detector [105] for the primary luminosity measurements.

When selecting events [106], the lowest unprescaled dilepton [107, 108] and $E_{\text{T}}^{\text{miss}}$ triggers [109] were used with a logical OR combination. For events with $E_{\text{T}}^{\text{miss}} < 250\,\text{GeV}$, only dilepton triggers were used, with lepton p_{T} thresholds varying throughout the Run 2 data-taking period up to a maximum of 24 GeV for triggers requiring two electrons, 22 GeV for the leading-p_{T} muon in triggers requiring two muons, and 17 GeV (14 GeV) for the electron (muon) in different-flavour dilepton triggers. For events with $E_{\text{T}}^{\text{miss}} > 250\,\text{GeV}$, dilepton triggers and $E_{\text{T}}^{\text{miss}}$ triggers were used. The above strategy is chosen to maximise the trigger efficiency, while selecting events relevant to the targeted final states [35]. The selection thresholds are defined such that the trigger efficiencies are constant throughout the lepton p_{T} and $E_{\text{T}}^{\text{miss}}$ range considered in the analysis.

Signal and background events produced in pp collisions were simulated with various Monte Carlo (MC) generators. They include the effect of multiple pp interactions in the same and neighbouring bunch crossings ('pile-up'), which was modelled by overlaying the hard-scattering event with simulated inelastic pp events generated by Pythia 8.186 [110, 111] with the the NNPDF2.3lo set of parton distribution functions (PDF) [112] and the A3 tune [113]. The MC events were weighted to reproduce the $\langle\mu\rangle$ distribution observed in the data. The EvtGen [114] program was used to simulate properties of the b- and c-flavoured hadron decays.

The detector response was simulated using either the full ATLAS detector description [115] based on Geant4 [116], or by fast simulation using a parameterisation of the performance of the electromagnetic and hadronic calorimeters and Geant4 for the other parts of the detector [117]. The generated events are reconstructed in the same manner as the data.

4.1 Signal samples

The signal samples of the targeted models were generated using MadGraph5_aMC@NLO v2.2.3 [1, 118] interfaced to Pythia 8.186 with the A14 tune [119] for the modelling of the parton showering (PS) [120], hadronisation and underlying event. The matrix element (ME) calculation was performed at tree-level including the emission of up to two additional partons. The PDF set used for the generation was NNPDF2.3lo [112]. The ME–PS matching was carried out using the CKKW-L prescription [121, 122],

with a matching scale set to one quarter of the pair-produced superpartner mass. For the bRPV model, the RPV parameters (together with the mass spectra and the decay modes) were determined by a fit to neutrino experimental data performed by the SPheno [123, 124] spectrum calculator produced by the Sarah [125, 126] package.

Signal cross sections were calculated to next-to-leading order (NLO) in the strong coupling constant, adding the resummation of soft gluon emission at next-to-leading-logarithmic (NLL) accuracy (NLO+NLL) using Resummino 2.0.1 [127–131]. The nominal cross section and the uncertainty were taken from an envelope of cross-section predictions using different PDF sets and factorisation and renormalisation scales [132, 133]. Production cross sections range between $O(10^{-3}$ pb) and $O(1$ pb).

4.2 Irreducible-background samples

WZ and $W^{\pm}W^{\pm}$ production represent the dominant irreducible background in most signal regions. Samples of fully leptonic, semileptonic and loop-induced VV ($V = W, Z$) and electroweak $VVjj$ processes were included. The associated production of a vector gauge boson with a $t\bar{t}$ pair, $t\bar{t}$+V, is also an important background. Depending on the targeted signal model, considerable background contributions come from $t\bar{t}$+H, tribosons and rare top processes, with the latter including tWZ, tZq and samples with three or four top quarks. Higgs boson production via vector-boson fusion (VBF) and in association with a vector boson (VH) was also considered, while production via gluon–gluon fusion was not included separately since the events are included in the diboson processes.

Samples of diboson final states VV were simulated with the Sherpa 2.2.2 [134] generator, including off-shell effects and Higgs boson contributions where appropriate. Fully leptonic final states and semileptonic final states, where one boson decays leptonically and the other hadronically, were generated using MEs at NLO accuracy in QCD for up to one additional parton and at leading-order (LO) accuracy for up to three additional parton emissions. Samples for the loop-induced processes $gg \rightarrow VV$ were generated using LO-accurate MEs for up to one additional parton emission for both the cases of fully leptonic and semileptonic final states. The ME calculations were matched and merged with the Sherpa PS based on Catani–Seymour (CS) dipole factorisation [135, 136] using the MEPS@NLO prescription [137–140]. The virtual QCD corrections were provided by the OpenLoops library [141–143]. The NNPDF3.0nnlo set of PDFs was used [144], along with the dedicated set of tuned PS parameters developed by the Sherpa authors.

Electroweak diboson production in association with two jets, $VVjj$, was simulated with the Sherpa 2.2.2 generator. The LO-accurate MEs were matched to the PS based on CS dipole factorisation using the MEPS@LO prescription. Samples were generated using the NNPDF3.0nnlo PDF set, along with the dedicated set of tuned PS parameters developed by the Sherpa authors.

The production of $t\bar{t}$+V events was modelled using the MadGraph5_aMC@NLO 2.3.3 [1] generator at NLO with the NNPDF3.0nlo [144] PDF. The events were interfaced to Pythia 8.210 [111] using the A14 tune and the NNPDF2.3lo [144] PDF set.

Higgs bosons produced in association with a $t\bar{t}$ pair, $t\bar{t}$+H, were generated using the Powheg Box v2 [145–149] generator at NLO with the NNPDF3.0nlo PDF set. The events were interfaced to Pythia 8.230 [111] using the A14 tune [119] and the NNPDF2.3lo PDF set.

Triboson (VVV) event production was simulated with the Sherpa 2.2.1 [134] generator. MEs accurate to LO in QCD for up to one additional parton emission were matched and merged with the Sherpa PS

based on CS dipole factorisation using the MEPS@LO prescription. Samples were generated using the NNPDF3.0NNLO PDF set, along with the dedicated set of tuned PS parameters developed by the SHERPA authors.

The production of rare top events was modelled using the MADGRAPH5_AMC@NLO 2.3.3 generator which provides MEs at NLO in the strong coupling constant α_s with the NNPDF3.1NLO [144] PDF. The functional form of the renormalisation and factorisation scales were set to $0.25\times\sum_i\sqrt{m_i^2+p_{\mathrm{T},i}^2}$, where the sum ran over all the particles generated from the ME calculation, following the Ref. [150]. Top quarks were decayed at LO using MADSPIN [151, 152] to preserve all spin correlations. The events were interfaced with PYTHIA 8.230 [111] for the PS and hadronisation, using the A14 set of tuned parameters and the NNPDF2.3LO PDF set.

The Higgs boson production was simulated with POWHEG BOX v2 [146–148, 153] and interfaced with PYTHIA 8 [111] for PS and non-perturbative effects. The POWHEG BOX prediction is accurate to NLO and uses the PDF4LHC15NLO PDF set [133] and the AZNLO tune [154] of PYTHIA 8 [111]. The loop-induced $gg \to ZH$ process was generated separately at LO. The MC prediction was normalised to cross sections calculated at next-to-NLO (NNLO) in QCD with NLO electroweak corrections for $q\bar{q}/qg \to VH$ and at NLO and NLL in QCD for $gg \to ZH$ [155–161]. The VBF production was normalised to an approximate-NNLO QCD cross section with NLO electroweak corrections [162–164]. The normalisation of all Higgs boson samples accounts for the decay branching ratio calculated with HDECAY [165–167] and PROPHECY4F [168–170].

4.3 Reducible-background samples

Even though they do not share the same final state as the signal, some SM processes are possible sources of background due to mis-identification of leptons or their charges. These *reducible* backgrounds, discussed in detail in Section 7, are estimated with data-driven techniques. They include QCD V+jets and electroweak VBF Vjj, as well as top-quark pairs and single-top events.

The production of QCD V+jets was simulated with the SHERPA 2.2.1 [134] generator using NLO MEs for up to two partons, and LO MEs for up to four partons calculated with the Comix [135] and OPENLOOPS [141–143] libraries. They were matched with the SHERPA parton shower [136] using the MEPS@NLO prescription [137–140] using the set of tuned parameters developed by the SHERPA authors. The NNPDF3.0NNLO set of PDFs [144] was used and the samples were normalised to a NNLO prediction [171].

Electroweak production of $\ell\ell jj$, $\ell\nu jj$ and $\nu\nu jj$ final states originating in electroweak VBF Vjj was simulated with SHERPA 2.2.11 [134] using LO MEs with up to one additional parton emission. The MEs were merged with the SHERPA PS [136] following the MEPS@LO prescription [139] and using the set of tuned parameters developed by the SHERPA authors. The NNPDF3.0NNLO set of PDFs [144] was employed. The samples were produced using the VBF approximation, which avoids overlap with semileptonic diboson topologies by requiring a t-channel colour-singlet exchange. The starting conditions of the CS shower are set according to the large-N_c amplitudes supplied by Comix [172] to achieve the correct VBF-appropriate radiation pattern.

The production of $t\bar{t}$ events was modelled using the POWHEG BOX v2 [145–148] generator at NLO with the NNPDF3.0NLO [144] PDF set and the h_{damp} parameter[2] set to $1.5\,m_{\text{top}}$ [173]. The events were interfaced to PYTHIA 8.230 [111] to model the PS, hadronisation, and underlying event, with parameters set according to the A14 tune [119] and using the NNPDF2.3LO set of PDFs [112].

The associated production of top quarks with W bosons (tW) and the single-top s-channel (t-channel) production were modelled using the POWHEG BOX v2 [146–148, 174, 175] generator at NLO in QCD in the five-flavour (four-flavour) scheme with the NNPDF3.0NLO [144] PDF set. For tW production, the diagram removal scheme [176] was used to remove interference and overlap with $t\bar{t}$ production. The events were interfaced with PYTHIA 8.230 [111] using the A14 tune [119] and the NNPDF2.3LO PDF set.

5 Object identification and reconstruction

Leptons and jets selected for analysis are categorised as 'baseline' (BL) or 'signal' (Sig) according to various quality and kinematic selection criteria. The baseline objects are used in the computation of $\mathbf{p}_{\text{T}}^{\text{miss}}$ and $E_{\text{T}}^{\text{miss}}$, defined below, and to resolve ambiguities between closely spaced analysis objects.

Electron candidates are reconstructed from energy depositions in the EM calorimeter matched to an ID track. The baseline electrons are required to satisfy the `Loose` identification [177] and to have $p_{\text{T}} > 10\,\text{GeV}$ and $|\eta| < 2.47$ with the LAr crack region ($1.37 < |\eta| < 1.52$) vetoed. The longitudinal impact parameter along the beam-line with respect to the primary vertex[3], z_0, of the electron track must satisfy $|z_0 \sin(\theta)| < 0.5\,\text{mm}$ and the transverse impact parameter, d_0, must be sufficiently small relative to its uncertainty from the track reconstruction, $|d_0/\sigma(d_0)| < 5$. Baseline electrons that satisfy the tighter `Medium` identification [177] and satisfy both a track-based and a calorimeter-based isolation criterion are selected as signal electrons. Track-based isolation requires the summed scalar p_{T} of nearby ID tracks not to exceed 6% of the electron p_{T}, for selected tracks in a p_{T}-dependent $\Delta R = \sqrt{(\Delta\eta)^2 + (\Delta\phi)^2}$ cone ($\Delta R = 10\,\text{GeV}/p_{\text{T}}$) of maximum size 0.2 around the electron, excluding its own track, similar to the isolation variables defined in Ref. [178]; these tracks must to be associated with the primary vertex to limit sensitivity to pile-up. Calorimeter-based isolation requires the sum of the transverse energy of the calorimeter energy clusters in a cone of $\Delta R = 0.2$ around the electron (excluding the energy from the lepton itself) to be less than 6% of that of the lepton. Only signal electrons with $|\eta| < 2.0$ are considered to suppress the contributions from electrons having misidentified charge, where the latter are further rejected by exploiting information related to the electron track reconstruction and its compatibility with the primary vertex and the electron cluster [177].

Muon candidates are reconstructed [178] in the region $|\eta| < 2.7$ from MS tracks matching ID tracks. Baseline muons are muons with $p_{\text{T}} > 10\,\text{GeV}$ and $|\eta| < 2.5$ satisfying the `Medium` requirements [179] and $|z_0 \sin(\theta)| < 0.5\,\text{mm}$. Signal muons are defined as baseline muons that also satisfy the requirement $|d_0/\sigma(d_0)| < 3$ and pass the pileup robust track-based isolation requirements, which are similar to the track-based isolation for electrons but with maximal cone size extended to 0.3.

Jets are reconstructed from particle-flow calorimeter clusters using the anti-k_t algorithm [180] with four-momentum recombination and distance parameter $R = 0.4$. The reconstructed jets are then calibrated by the application of a jet energy scale derived from 13 TeV data and simulation [181]. Jets with $p_{\text{T}} > 20$ GeV and $|\eta| < 2.5$ (central jets), or $p_{\text{T}} > 30$ GeV and $|\eta| < 4.5$ (forward jets) are used as baseline jets in the

[2] The h_{damp} parameter is a resummation damping factor and one of the parameters that controls the matching of POWHEG MEs to the PS and thus effectively regulates the high-p_{T} radiation against which the $t\bar{t}$ system recoils.

[3] The primary vertex is defined as the one with the largest sum of track p_{T}^2.

analysis and are further used to compute $E_{\mathrm{T}}^{\mathrm{miss}}$. Signal jets are selected as jets satisfying the requirements of $p_{\mathrm{T}} > 20\,\mathrm{GeV}$ and $|\eta| < 2.8$. To suppress jets originating from pile-up, additional track-based criteria are applied by using the `Tight` working point of the jet vertex tagger [181, 182].

Signal jets containing b-hadrons, referred to as b-jets, are identified *(b-tagged)* by the `DL1r` algorithm [183, 184] via a multivariate discriminant combining information from the impact parameters of displaced tracks with topological properties of secondary and tertiary decay vertices reconstructed within the jet. The chosen working point has a b-jet tagging efficiency of 70% and rejection factors of 6 and 134 for charm-jets and light-jets, respectively. Additionally, the selected b-jets must satisfy $|\eta| < 2.5$.

To avoid the double counting of analysis baseline objects, a procedure to remove reconstruction ambiguities is applied as follows:

- Electron candidates within $\Delta R' = \sqrt{(\Delta y)^2 + (\Delta\phi)^2} = 0.01$ of a muon are removed.[4] Softer electron candidates are removed if they are within $\Delta R' = 0.05$ of other electron candidates.
- Jet candidates within $\Delta R' = 0.2$ of an electron candidate are removed unless the jet candidate is a b-jet and with $p_{\mathrm{T}} < 100\,\mathrm{GeV}$. Jets with fewer than three tracks that lie within $\Delta R' = 0.4$ of a muon candidate are removed.
- Subsequently, electrons and muons within $\Delta R' = \min\{0.4, 0.1 + 9.6\,\mathrm{GeV}/p_{\mathrm{T}}(\ell)\}$ of a jet candidate are removed to reject non-prompt or fake leptons originating from hadron decays.

The $\mathbf{p}_{\mathrm{T}}^{\mathrm{miss}}$ is defined as the negative vector sum of the transverse momenta of all identified objects (baseline electrons, photons [177], muons and jets) and an additional soft term. The soft term is constructed from all tracks associated with the primary vertex but not with any leptons or jets. In this way, the $E_{\mathrm{T}}^{\mathrm{miss}}$ is adjusted for the best calibration of the jets and the other identified physics objects listed above, while maintaining approximate pile-up independence in the soft term [185, 186]. Overlaps between objects in the $E_{\mathrm{T}}^{\mathrm{miss}}$ calculation are resolved as described in Ref. [185].

6 Analysis strategy and event selection

After a basic event-cleaning procedure is applied, events are required to have a primary vertex with at least two associated tracks with $p_{\mathrm{T}} > 500\,\mathrm{MeV}$. Jets likely to be produced by beam-induced backgrounds, cosmic rays or detector noise are removed and other jet quality criteria are imposed [187]. Events with at least one muon with low momentum resolution are rejected.

Events with at least two signal leptons, with the leading lepton satisfying $p_{\mathrm{T}} > 20\,\mathrm{GeV}$, are selected. In addition, there must be either at least one pair of leptons with identical electric charges among the ensemble of signal leptons or exactly three leptons. The presence of at least one jet is also required in most SRs to improve the selection of signal events and to specifically target compressed-spectra regions. To distinguish between hypothetical SUSY signal processes and SM backgrounds, sets of signal regions (SRs) are designed optimised for the SUSY models defined in Section 2. Each of these SRs, described in Tables 1 to 3, is kept orthogonal to other ATLAS analyses [56] to facilitate future statistical combinations. Several kinematic variables are deployed to maximise the sensitivities to the targeted signals.

[4] The symbol y denotes the rapidity of an object.

Table 1: Signal region definitions designed for the Wh model. The variables are defined in the text.

	$\mathrm{SR}^{Wh}_{\mathrm{high}-m_{\mathrm{T2}}}$			$\mathrm{SR}^{Wh}_{\mathrm{low}-m_{\mathrm{T2}}}$		
	$e^{\pm}e^{\pm}$	$e^{\pm}\mu^{\pm}$	$\mu^{\pm}\mu^{\pm}$	$e^{\pm}e^{\pm}$	$e^{\pm}\mu^{\pm}$	$\mu^{\pm}\mu^{\pm}$
$N_{\mathrm{BL}}(\ell)$	$= 2$					
$N_{\mathrm{Sig}}(\ell)$	$= 2$					
Charge(ℓ)	same-sign					
$p_{\mathrm{T}}(\ell)$	≥ 25 GeV					
n_{jets} ($p_{\mathrm{T}} > 25$ GeV)	≥ 1					
$n_{b\text{-jets}}$	$= 0$					
m_{jj}	< 350 GeV					
m_{T2}	≥ 80 GeV			< 80 GeV		
$m_{\mathrm{T}}^{\mathrm{min}}$	–			≥ 100 GeV		
$\mathcal{S}(E_{\mathrm{T}}^{\mathrm{miss}})$	≥ 7			≥ 6		
$E_{\mathrm{T}}^{\mathrm{miss}}$	≥ 75 GeV			≥ 50 GeV		
$E_{\mathrm{T}}^{\mathrm{miss}}$ binning (GeV)[a]	$\mathrm{SR}^{Wh}_{\mathrm{high}-m_{\mathrm{T2}}}$-1: $\in [75, 125)$ $\mathrm{SR}^{Wh}_{\mathrm{high}-m_{\mathrm{T2}}}$-2: $\in [125, 175)$ $\mathrm{SR}^{Wh}_{\mathrm{high}-m_{\mathrm{T2}}}$-3: $\in [175, +\infty)$			–		

[a] The $E_{\mathrm{T}}^{\mathrm{miss}}$ binning applies separately to each flavour channel of $\mathrm{SR}^{Wh}_{\mathrm{high}-m_{\mathrm{T2}}}$.

The 'stransverse mass', m_{T2}, is an event variable used to bound the masses of an unseen pair of particles which are presumed to have decayed semi-invisibly into particles which were seen. Therefore, it is defined as a function of the momenta of two visible particles and the $\mathbf{p}_{\mathrm{T}}^{\mathrm{miss}}$ of the event:

$$m_{\mathrm{T2}} = \min_{\mathbf{q}_{\mathrm{T}}} \left[\max \left(m_{\mathrm{T},\ell_1}(\mathbf{p}_{\mathrm{T},\ell_1}, \mathbf{q}_{\mathrm{T}}), m_{\mathrm{T},\ell_2}(\mathbf{p}_{\mathrm{T},\ell_2}, \mathbf{p}_{\mathrm{T}}^{\mathrm{miss}} - \mathbf{q}_{\mathrm{T}}) \right) \right], \tag{2}$$

where $\mathbf{p}_{\mathrm{T},\ell_1}$ and $\mathbf{p}_{\mathrm{T},\ell_2}$ are the transverse momenta of the two leading leptons, and $\mathbf{q}_{\mathrm{T}}$ is the transverse momentum vector that minimises the larger of the two transverse masses m_{T,ℓ_1} and m_{T,ℓ_2}. The latter masses are defined as

$$m_{\mathrm{T}}(\mathbf{p}_{\mathrm{T}}, \mathbf{q}_{\mathrm{T}}) = \sqrt{2(p_{\mathrm{T}} q_{\mathrm{T}} - \mathbf{p}_{\mathrm{T}} \cdot \mathbf{q}_{\mathrm{T}})}. \tag{3}$$

In this analysis, the invisible particle mass is always set to zero when calculating the event m_{T2}.

For the Wh and WZ models, requiring the invariant mass of the two leading jets, m_{jj}, to be less than 350 GeV[5], proved to be efficient in reducing the $W^{\pm}W^{\pm}$ background. The minimum transverse mass, $m_{\mathrm{T}}^{\mathrm{min}}$, between the two leading leptons and the $\mathbf{p}_{\mathrm{T}}^{\mathrm{miss}}$ is used to recover the sensitivity which would be otherwise lost if only high m_{T2} were considered. The $E_{\mathrm{T}}^{\mathrm{miss}}$ and its significance, $\mathcal{S}(E_{\mathrm{T}}^{\mathrm{miss}})$[6] [188], which quantifies the robustness of the $E_{\mathrm{T}}^{\mathrm{miss}}$ values against object mis-measurements in events lacking a genuine source of $E_{\mathrm{T}}^{\mathrm{miss}}$, are also used aiming at the large $E_{\mathrm{T}}^{\mathrm{miss}}$ induced by the (invisible) LSP in RPC scenarios. The angular distance between the two SS leptons, $\Delta R(\ell^{\pm}, \ell^{\pm})$, is used only for the WZ model since the SS leptons are

[5] If the event has only one jet, m_{jj} was set to zero.

[6] $\mathcal{S}(E_{\mathrm{T}}^{\mathrm{miss}}) = \frac{|E_{\mathrm{T}}^{\mathrm{miss}}|^2}{\sigma_L^2(1-\rho_{LT}^2)}$, with σ_L^2 the total variance in the longitudinal direction along $\mathbf{p}_{\mathrm{T}}^{\mathrm{miss}}$ and ρ_{LT}^2 the correlation between the longitudinal and transverse resolutions of the objects.

Table 2: Signal region definitions designed for WZ model. The variables are defined in the text.

	$\mathrm{SR}^{WZ}_{\mathrm{high}-m_{\mathrm{T2}}}$	$\mathrm{SR}^{WZ}_{\mathrm{low}-m_{\mathrm{T2}}}$
$N_{\mathrm{BL}}(\ell)$	$= 2$	
$N_{\mathrm{Sig}}(\ell)$	$= 2$	
Charge(ℓ)	same-sign	
$p_{\mathrm{T}}(\ell)$	≥ 25 GeV	
n_{jets} $(p_{\mathrm{T}} > 25$ GeV$)$	≥ 1	
$n_{b\text{-jets}}$	$= 0$	
m_{jj}	≤ 350 GeV	
m_{T2}	≥ 100 GeV	≤ 100 GeV
$m_{\mathrm{T}}^{\mathrm{min}}$	≥ 100 GeV	≥ 130 GeV
$E_{\mathrm{T}}^{\mathrm{miss}}$	≥ 100 GeV	≥ 140 GeV
m_{eff}	–	≤ 600 GeV
$\Delta R(\ell^{\pm}, \ell^{\pm})$	–	≤ 3
Bins	$\mathcal{S}(E_{\mathrm{T}}^{\mathrm{miss}})$: $\in [0, 10)$ Spread$(\Phi) \geq 2.2$	–
	$\mathcal{S}(E_{\mathrm{T}}^{\mathrm{miss}})$: $\in [10, 13)$	
	$\mathcal{S}(E_{\mathrm{T}}^{\mathrm{miss}})$: $\in [13, +\infty]$ $\Delta R(\ell^{\pm}, \ell^{\pm}) \geq 1$	

Table 3: Signal region definitions designed for bRPV model. The variables are defined in the text.

	$\mathrm{SR}^{\mathrm{bRPV}}_{2\ell-\mathrm{SS}}$	$\mathrm{SR}^{\mathrm{bRPV}}_{3\ell}$
$N_{\mathrm{BL}}(\ell)$	–	
p_{T} (ℓ)	≥ 20 GeV for (sub)leading leptons	
n_{jets} $(p_{\mathrm{T}} > 25$ GeV$)$	≥ 1	
$N_{\mathrm{Sig}}(\ell)$	$= 2$	$= 3$
Charge(ℓ)	same-sign	–
m_{T2}	≥ 60 GeV	≥ 80 GeV
$E_{\mathrm{T}}^{\mathrm{miss}}$	≥ 100 GeV	≥ 120 GeV
m_{eff}	–	≥ 350 GeV
$n_{b\text{-jets}}$	$= 0$	–
n_{jets} $(p_{\mathrm{T}} > 40$ GeV$)$	≥ 4	–
$m_{e^{\pm}e^{\mp}}$, $m_{\mu^{\pm}\mu^{\mp}}$	–	$\notin [81, 101]$ GeV

coming from two decay legs and should not be too separated when the mass of the SUSY particles are similar.

A multi-bin strategy is applied in the SRs for the two wino-bino models using the $E_{\mathrm{T}}^{\mathrm{miss}}$ and the SS lepton-pair flavour or $\mathcal{S}(E_{\mathrm{T}}^{\mathrm{miss}})$ to maximise the sensitivity across the model phase space. For the bins

defined for $\mathrm{SR}^{WZ}_{\mathrm{high}-m_{\mathrm{T2}}}$, requirements on the Spread(Φ)[7] or $\Delta R(\ell^{\pm}, \ell^{\pm})$ are applied to further improve the sensitivities to the benchmark model. The Wh SRs are divided in different flavour channels to maximise the analysis power.

For the bRPV model, large $E_{\mathrm{T}}^{\mathrm{miss}}$ is expected due to the presence of a neutrino in the leptonic decay of the W boson. High jet multiplicity is required in the two-SS-lepton SR to improve the sensitivity to possible hadronic decays of the higgsinos and the W. The m_{T2} threshold at 60 GeV or 80 GeV is found to be helpful due to the different compositions of the $E_{\mathrm{T}}^{\mathrm{miss}}$ between the signal and the background sources. The lower boundary of effective mass, m_{eff}, defined as the scalar sum of the objects p_{T} and $E_{\mathrm{T}}^{\mathrm{miss}}$, at 350 GeV, has also proven useful to reduce the background for the three-lepton SR after the Z-boson veto ($m_{e^{\pm}e^{\mp}},\ m_{\mu^{\pm}\mu^{\mp}} \notin [81, 101]$ GeV) and the b-jet veto is applied to further reduce the $t\bar{t}$ backgrounds for the two-SS-lepton SR.

Within each signal model, the SRs are designed to be orthogonal to allow their statistical combination in the interpretation of the results. In the wino-bino models, this is achieved with the m_{T2} variable, while the number of signal leptons, $N_{\mathrm{Sig}}(\ell)$, ensures orthogonality in the bRPV model.

While these SRs are designed to maximise the sensitivity to specific benchmark models, a different set of *discovery SRs* has been defined to enhance the discovery potential for a variety of BSM scenarios, such as simplified models with electroweak SUSY production which span from compressed to high mass-splitting scenarios. The inclusive $\mathrm{SR}^{Wh}_{\mathrm{high}-m_{\mathrm{T2}}}$ and $\mathrm{SR}^{Wh}_{\mathrm{low}-m_{\mathrm{T2}}}$ for the Wh and the $\mathrm{SR}^{WZ}_{\mathrm{high}-m_{\mathrm{T2}}}$ and $\mathrm{SR}^{WZ}_{\mathrm{low}-m_{\mathrm{T2}}}$ for the WZ models defined without any $E_{\mathrm{T}}^{\mathrm{miss}}$ or $\mathcal{S}(E_{\mathrm{T}}^{\mathrm{miss}})$ binning or flavour splitting act as such discovery regions.

7 Background estimation

The treatment of the SM backgrounds is based on their classification into irreducible backgrounds, coming from processes with genuine same-sign prompt leptons, and reducible backgrounds, with events which enter into the SRs due to mis-identification of the lepton ('fake/non-prompt') or the lepton charge ('charge-flip'). The 'charge-flip' events (denoted in the following as CF events) are caused by the emission of a bremsstrahlung photon which through interaction with detector material converts into a pair of secondary electron tracks. Among those tracks, one of them happens to better match the position of the calorimeter cluster than the original electron track and has a charge opposite to that of the prompt electron. The CF contribution coming from muons is negligible due to the small cross section of interaction with matter. The 'fake/non-prompt' events (denoted in the following as FNP events) are mainly produced in heavy-flavour meson decays, converted photons from various origins, light hadrons faking the electron shower, and in-flight decays of kaons or pions to muons. Lepton candidates reconstructed from these different sources share the properties of being generally not well isolated and being mostly rejected by the lepton identification criteria and impact parameter requirements.

The dominant irreducible processes in the SRs defined in this analysis are WZ, $W^{\pm}W^{\pm}$ for b-jet-vetoing SRs ($\mathrm{SR}^{Wh}_{\mathrm{high}-m_{\mathrm{T2}}}$, $\mathrm{SR}^{Wh}_{\mathrm{low}-m_{\mathrm{T2}}}$, $\mathrm{SR}^{WZ}_{\mathrm{high}-m_{\mathrm{T2}}}$, $\mathrm{SR}^{WZ}_{\mathrm{low}-m_{\mathrm{T2}}}$ and $\mathrm{SR}^{\mathrm{bRPV}}_{2\ell-\mathrm{SS}}$) and $t\bar{t}+V$ for the b-jet-agnostic SR ($\mathrm{SR}^{\mathrm{bRPV}}_{3\ell}$). Their contribution to the respective SRs is evaluated by employing data-driven background

[7] The spread of the Φ angles of the leptons, $E_{\mathrm{T}}^{\mathrm{miss}}$, and jets is used to describe the event topology in the transverse plane. It is defined as: $\mathrm{Spread}(\Phi) = \frac{\mathcal{R}(\phi_{\ell 1},\ \phi_{\ell 2},\ \phi_{E_{\mathrm{T}}^{\mathrm{miss}}})\cdot\mathcal{R}(\phi_{j1},\ \phi_{j2},\dots)}{\mathcal{R}(\phi_{\ell 1},\ \phi_{\ell 2},\ \phi_{E_{\mathrm{T}}^{\mathrm{miss}}},\ \phi_{j1},\ \phi_{j2},\dots)}$, where $\mathcal{R}$ means the root-mean-square of the inputs.

Table 4: Control region and validation region definitions for evaluating and validating the dominant irreducible backgrounds in SRs defined for the Wh model.

	$\mathrm{CR}WZ^{Wh}$	$\mathrm{VR}WZ^{Wh}$	$\mathrm{CR}WW^{Wh}$	$\mathrm{VR}WW^{Wh}$
$N_{\mathrm{BL}}(\ell)$	$= 3$		$= 2$	
$N_{\mathrm{Sig}}(\ell)$			$= 2$	
$\mathrm{Charge}(\ell)$			same-sign	
$p_{\mathrm{T}}(\ell)$			$\geq 25\,\mathrm{GeV}$	
$n_{b\text{-jets}}$			$= 0$	
$E_{\mathrm{T}}^{\mathrm{miss}}$			$\geq 50\,\mathrm{GeV}$	
n_{jets}	≥ 1		≥ 2	
$\mathcal{S}(E_{\mathrm{T}}^{\mathrm{miss}})$	< 6	≥ 6	< 6	≥ 6
Other cuts	$75 < m_{\mathrm{SFOS}} < 105\,\mathrm{GeV}$		–	
	$m_{\ell\ell\ell} \notin [80, 100]\,\mathrm{GeV}$		–	
	–		$m_{jj} \geq 350\,\mathrm{GeV}$	
	–		$p_{\mathrm{T}}(\mathrm{jets}) \geq 75\,\mathrm{GeV}$ for (sub)leading jets	
	–		$\lvert m_{e^{\pm}e^{\pm}} - m_Z \rvert \geq 15\,\mathrm{GeV}$	
Purity	90%	90%	45%	55%

estimation techniques based on measurements made in control regions (CRs); the same strategy is followed for the reducible background sources. All other irreducible processes, discussed in Section 4, are estimated with the aid of MC simulation.

The background estimates are obtained by performing a profile log-likelihood fit [189], implemented in the HistFitter [190] software framework, considering only the CRs and assuming no signal presence. The statistical and systematic uncertainties are implemented as nuisance parameters in the likelihood; Poisson constraints are used to estimate the uncertainties arising from limited numbers of events in the MC samples, whilst Gaussian constraints are used for experimental and theoretical systematic uncertainties. The normalisation factors and nuisance parameters are adjusted by maximising the likelihood. The significance of the difference between the observed and expected yields is calculated with the profile likelihood method [191], adding a minus sign if the yield is below the prediction.

The validation regions (VRs), which solely serve to validate the background estimation in the SRs, are defined in a way to be close to both the SRs and the CRs. The background prediction as obtained from this background-only fit is compared with data in the VRs to assess the quality of the background modelling.

For the dominant backgrounds in SRs designed for the Wh model ($\mathrm{SR}^{Wh}_{\mathrm{high}-m_{\mathrm{T2}}}$ and $\mathrm{SR}^{Wh}_{\mathrm{low}-m_{\mathrm{T2}}}$), dedicated CRs for the WZ ($\mathrm{CR}WZ^{Wh}$) and the $W^{\pm}W^{\pm}$ process ($\mathrm{CR}WW^{Wh}$) are designed separately to be very close to the SRs. The correction factors for the particular background process targeted by the specific control regions are obtained with a simultaneous fit in the specific control regions. Corresponding validation regions (VRs) with enriched contributions from WZ ($\mathrm{VR}WZ^{Wh}$) or $W^{\pm}W^{\pm}$ ($\mathrm{VR}WW^{Wh}$) are also defined to validate the estimation. The definitions of $\mathrm{CR}WZ^{Wh}$, $\mathrm{CR}WW^{Wh}$, $\mathrm{VR}WZ^{Wh}$ and $\mathrm{VR}WW^{Wh}$ are listed in Table 4.

Similar requirements on the number of leptons, $N_{\mathrm{Sig}}(\ell)$ and $N_{\mathrm{BL}}(\ell)$, number of jets, n_{jets}, and $E_{\mathrm{T}}^{\mathrm{miss}}$ to

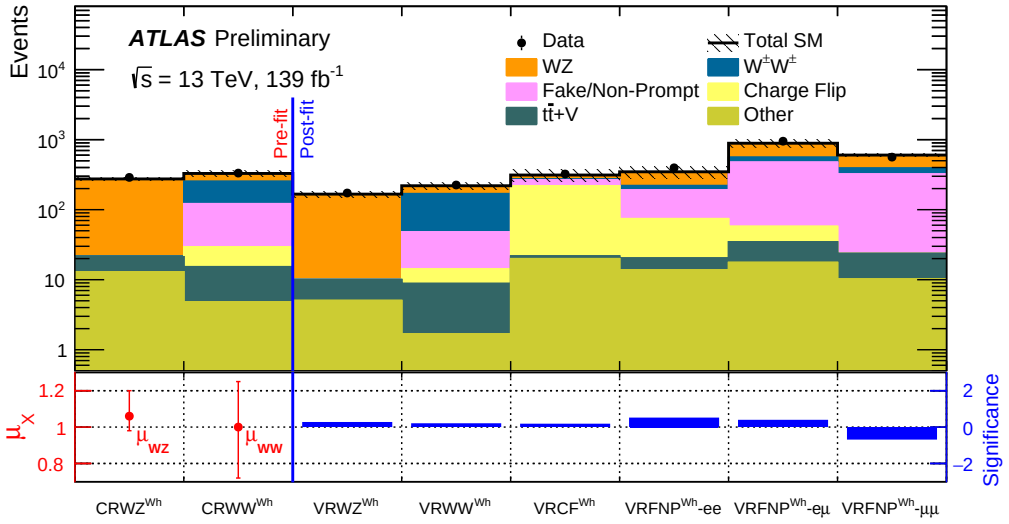

Figure 3: Expected SM backgrounds and data yields in the CRWZ^{Wh}, CRWW^{Wh}, VRWZ^{Wh}, VRWW^{Wh}, VRCF^{Wh} and VRFNP^{Wh} designed for the Wh model. The 'Other' category contains the $t\bar{t}$+H, rare top, triboson, and other diboson processes with the SS final state. The error band includes the statistical, theoretical and experimental uncertainties. The bottom panel shows the obtained scale factors (μ_{WZ}, μ_{WW}) in the CRs and the statistical significance [191] of the discrepancy between the observed number of events and the SM expectation.

$\mathrm{SR}^{Wh}_{\mathrm{high}-m_{\mathrm{T2}}}$ and $\mathrm{SR}^{Wh}_{\mathrm{low}-m_{\mathrm{T2}}}$ are applied to the CRs and VRs, listed in Table 4. The significance of $E_{\mathrm{T}}^{\mathrm{miss}}$ ($\mathcal{S}(E_{\mathrm{T}}^{\mathrm{miss}})$) larger or smaller than six is used to distinguish the CRs from VRs while maintaining the VRs close to the SRs. For WZ-enriched regions, the third lepton satisfies the baseline lepton criteria *without* fulfilling the signal lepton definition to keep the orthogonality between CRs, VRs and SRs. Additional requirements are set on the invariant mass of a pair of same-flavour opposite-sign leptons (SFOS), m_{SFOS}, to be within a window of 15 GeV around m_Z, and on the invariant mass of the three leptons, $m_{\ell\ell\ell}$, to be away from the Z mass peak. Such criteria further improve the purity and suppress other backgrounds. The purity of WZ process in CRWZ^{Wh} and VRWZ^{Wh} is about 90% with negligible contamination from signal.

For regions enriched with the $W^{\pm}W^{\pm}$ process, two boosted jets with $p_{\mathrm{T}} \geq 75$ GeV are required to target the $W^{\pm}W^{\pm}$ process, and together with the $m_{jj} \geq 350$ GeV requirement, the orthogonality with respect to the SRs is also preserved. To suppress the CF contribution, events are rejected if $|m_{e^{\pm}e^{\pm}} - m_Z| < 15$ GeV. The final purity of CRWW^{Wh} (VRWW^{Wh}) is about 45% (55%) with a signal contamination of less than 3% in both the CR and the VR. The correction factors are $1.06^{+0.14}_{-0.08}$ and $1.00^{+0.25}_{-0.28}$ for the WZ and $W^{\pm}W^{\pm}$ backgrounds, respectively, and are applied to these background events in the regions designed for the Wh model. Both statistical and systematic uncertainties are considered in the corrections factors. From Figure 3, a good agreement between the observed data and the estimated backgrounds can be seen for VRWZ^{Wh} and VRWW^{Wh}.

For SRs designed for the WZ model and models of higgsino-like electroweakinos in RPV considered in this analysis, a general control region CR$WZ_{2j}^{WZ,(\mathrm{b})\mathrm{RPV}}$ for the WZ process is defined to correct the cross section of this process in a phase space with at least two jets, where an imprecise modelling was observed in

Table 5: Control region and validation region definitions for evaluating and validating the dominant irreducible backgrounds in SRs defined for the WZ model and models of higgsino-like electroweakinos in RPV.

	$\mathrm{CR}WZ_{2j}^{WZ,(\mathrm{b})\mathrm{RPV}}$	$\mathrm{VR}WZ_{4j}^{WZ,(\mathrm{b})\mathrm{RPV}}$	$\mathrm{VR}WZ_{5j}^{WZ,(\mathrm{b})\mathrm{RPV}}$	$\mathrm{VR}t\bar{t}V^{WZ,(\mathrm{b})\mathrm{RPV}}$
$N_{\mathrm{BL}}(\ell)$	$= 3$			≥ 2
$N_{\mathrm{Sig}}(\ell)$	$= 3$			≥ 2
Charge(ℓ)	–			same-sign
$p_{\mathrm{T}}(\ell)$	$p_{\mathrm{T}} > 20\,\mathrm{GeV}$ for (sub)leading leptons			$p_{\mathrm{T}} > 30\,\mathrm{GeV}$ for SS pair leptons
$n_{b\text{-jets}}$	$= 0$			≥ 1
n_{jets} ($p_{\mathrm{T}} \geq 25\,\mathrm{GeV}$)	≥ 2	≥ 4	≥ 5	≥ 3 with $p_{\mathrm{T}} > 40\,\mathrm{GeV}$
Other selections	$50 < E_{\mathrm{T}}^{\mathrm{miss}} < 150\,\mathrm{GeV}$	$50 < E_{\mathrm{T}}^{\mathrm{miss}} < 250\,\mathrm{GeV}$		–
	$m_{\mathrm{eff}} < 1\,\mathrm{TeV}$	$m_{\mathrm{eff}} < 1.5\,\mathrm{TeV}$		–
	$81 < m_{\mathrm{SFOS}} < 101\,\mathrm{GeV}$	$81 < m_{\mathrm{SFOS}} < 101\,\mathrm{GeV}$		–
	–			$\Delta R(\ell_1, jet)_{\mathrm{min}} > 1.1$
	–			$\sum p_{\mathrm{T}}^{b\text{-jet}} / \sum p_{\mathrm{T}}^{\mathrm{jet}} > 0.4$
	–			$E_{\mathrm{T}}^{\mathrm{miss}} / m_{\mathrm{eff}} > 0.1$
	vetoing $\mathrm{SR}_{\mathrm{high}-m_{\mathrm{T2}}}^{WZ}$ & $\mathrm{SR}_{\mathrm{low}-m_{\mathrm{T2}}}^{WZ}$ & $\mathrm{SR}_{2\ell-\mathrm{SS}}^{\mathrm{bRPV}}$ & $\mathrm{SR}_{3\ell}^{\mathrm{bRPV}}$ events			
	vetoing other possible BSM events			
	$n_{b\text{-jets}} \geq 3$			
	$n_{b\text{-jets}} \geq 1$, $n_{\mathrm{jets}} \geq 4$ ($p_{\mathrm{T}} > 50\,\mathrm{GeV}$), $E_{\mathrm{T}}^{\mathrm{miss}} > 130\,\mathrm{GeV}$			
	$n_{b\text{-jets}} = 0$, $n_{\mathrm{jets}} \geq 3$ ($p_{\mathrm{T}} > 50\,\mathrm{GeV}$), $E_{\mathrm{T}}^{\mathrm{miss}} > 130\,\mathrm{GeV}$			
	$n_{b\text{-jets}} = 0$, $n_{\mathrm{jets}} \geq 5$ ($p_{\mathrm{T}} > 50\,\mathrm{GeV}$)			
Purity	85%	84%	77%	62%

previous studies [35]. The validation regions for the WZ process ($\mathrm{VR}WZ_{4j}^{WZ,(\mathrm{b})\mathrm{RPV}}$ and $\mathrm{VR}WZ_{5j}^{WZ,(\mathrm{b})\mathrm{RPV}}$) and for the $t\bar{t}V$ process ($\mathrm{VR}t\bar{t}V^{WZ,(\mathrm{b})\mathrm{RPV}}$), defined in Table 5, are designed to validate the estimations from the MC simulation of these processes.

Requirements are placed on the number of signal leptons, $N_{\mathrm{Sig}}(\ell)$, baseline leptons, $N_{\mathrm{BL}}(\ell)$, the number of jets, n_{jets}, and the number of b-jets, $n_{b\text{-jets}}$. Additional requirements are set on $E_{\mathrm{T}}^{\mathrm{miss}}$, m_{eff}, m_{SFOS} and the presence of SS leptons. A minimum angular separation between the leading lepton and the jets, $\Delta R(\ell_1, j)_{\mathrm{min}}$, is applied in the validation regions targeting $t\bar{t}+V$ events, as well as requirements on $\sum p_{\mathrm{T}}^{b\text{-jet}} / \sum p_{\mathrm{T}}^{\mathrm{jet}}$. The leading and sub-leading lepton p_{T} is required to be above 20 GeV. The events belonging to the SRs of the WZ model and the bRPV model defined in Section 6 are vetoed. In addition, the selections given in Table 5 are applied to ensure a more stringent rejection of bRPV and UDD RPV possible signal events, as well as other SUSY signals with several (b-)jets and moderate $E_{\mathrm{T}}^{\mathrm{miss}}$ in the final state. These vetoes help to reduce the expected signal contamination to a few percent. The purity for the target background process varies from a minimum of 62% ($\mathrm{VR}t\bar{t}V^{WZ,(\mathrm{b})\mathrm{RPV}}$) to a maximum of 85% ($\mathrm{CR}WZ_{2j}^{WZ,(\mathrm{b})\mathrm{RPV}}$).

The correction factor and its uncertainty are extracted from the $\mathrm{CR}WZ_{2j}^{WZ,(\mathrm{b})\mathrm{RPV}}$ and are found to be 0.88 ± 0.30. The estimated backgrounds and the observed data for the $\mathrm{CR}WZ_{2j}^{WZ,(\mathrm{b})\mathrm{RPV}}$, $\mathrm{VR}WZ_{4j}^{WZ,(\mathrm{b})\mathrm{RPV}}$, $\mathrm{VR}WZ_{5j}^{WZ,(\mathrm{b})\mathrm{RPV}}$ and $\mathrm{VR}t\bar{t}V^{WZ,(\mathrm{b})\mathrm{RPV}}$ are shown in Figure 4, where good agreement is observed.

The contributions of the CF events are evaluated from reweighted data events with two opposite-sign leptons ($e^{\pm}e^{\mp}$, $e^{\pm}\mu^{\mp}$). The weight used for reweighting indicates the probability of one electron charge to be mis-measured and is a function of the electron CF rates. This method largely improves the statistical

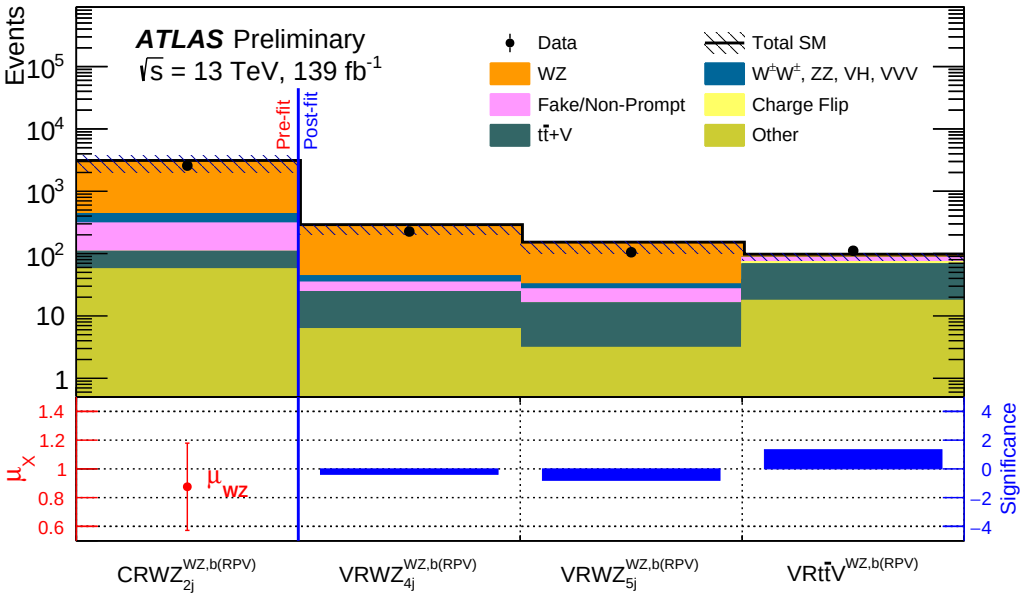

Figure 4: Expected SM backgrounds and data yields in the CR$WZ_{2j}^{WZ,(b)RPV}$, VR$WZ_{4j}^{WZ,(b)RPV}$, VR$WZ_{5j}^{WZ,(b)RPV}$ and VR$t\bar{t}V^{WZ,(b)RPV}$ designed for the WZ model and models of higgsino-like electroweakinos in RPV. The 'Other' category contains the $t\bar{t}$+H and rare top processes with the SS final state. The error band includes the statistical, theoretical and experimental uncertainties. The bottom pad shows the obtained scale factor from CR$WZ_{2j}^{WZ,(b)RPV}$ (μ_{WZ}) and the statistical significance [191] of the discrepancy between the observed number of events and the SM expectation.

accuracy by relying entirely on the data for these backgrounds and eliminating the associated experimental and theoretical uncertainties due to MC simulations. An additional 25% uncertainty stems from the choice of the lepton selections, and was derived by comparing the nominal CF predictions with those obtained using BL leptons.

The CF rates are measured as a function of leptons p_{T} and $|\eta|$ for simulated SM processes that contribute to the SRs due to CF. They are further multiplied by the scale factors obtained from a 'tag and probe' method [177] to match the rates observed in data. The nominal CF rates are within $O(10^{-6})$ in the low-p_{T} region and reaching to $O(1\%)$ at the higher p_{T} and $|\eta|$ regions. Systematic uncertainties are estimated from statistical uncertainties of the measured CF rates and the uncertainties from the scale factors, leading to a 10% to 40% uncertainty in the predicted SR yields for the CF background.

The fake-factor method, the matrix method and the MC template method are used in this analysis to estimate the contributions of the FNP events in the SRs. Both the fake-factor and the matrix methods are purely data-driven methods, which are commonly employed in the ATLAS collaboration [192–194] to estimate the FNP background in dedicated regions. In this analysis, the fake-factor method is used to estimate the contribution of FNP events in the Wh regions. Hence, the measurements of the values of the fake-factors are specifically tailored to reflect the FNP composition of the two-SS leptons SRs of the Wh model. The implementation of the matrix method in this analysis is instead designed to have greater universality, which enables it to estimate the FNP contribution in more complex regions. Therefore, it is used to evaluate the FNP events for SRs defined for the WZ model and models of higgsino-like electroweakinos in RPV which have two SS leptons, three leptons, b-vetoed, and b-favoured channels. Finally, the (semi data-driven)

Table 6: Definitions of the FNP-enriched control regions used to measure the FFs and the definitions of the validation regions for validating the estimations of the FNP and CF events in SRs defined for the Wh model.

	CRFF_e	CRFF_μ	VRFNP^{Wh}			VRCF^{Wh}
	$e^\pm e^\pm$	$\mu^\pm\mu^\pm$	$e^\pm e^\pm$	$e^\pm\mu^\pm$	$\mu^\pm\mu^\pm$	$e^\pm e^\pm$
$N_{\text{BL}}(\ell)$	= 2					
Charge(ℓ)	same-sign					
$N_{\text{Sig}}(\ell)$	= 1		= 2			
$p_{\text{T}}(\ell)$	$\geq$ 25 GeV					
n_{jets}	$\geq$ 1					
$n_{b\text{-jets}}$	–	= 1	= 0			
$E_{\text{T}}^{\text{miss}}$	$\in$ [30, 50) GeV	$<$ 50 GeV	$\geq$ 50 GeV			
$\lvert m_{\ell^\pm\ell^\pm} - m_Z\rvert$	$\geq$ 15 GeV	–	$\geq$ 15 GeV	–	–	$<$ 15 GeV
m_{jj}	–		$<$ 350 GeV			
m_{T2}	–		$<$ 80 GeV			
$m_{\text{T}}^{\text{min}}$	–		$<$ 100 GeV			
$\mathcal{S}(E_{\text{T}}^{\text{miss}})$	–		$<$ 5			

MC template method [39] is used for validating specific matrix-method estimations to ensure that the extrapolation of the universality of the matrix method to the specific cases in this analysis is functioning well.

The fake-factor method estimates the FNP events in a specific region by reweighting events passing the same selection except for inverted lepton identification and/or isolation requirements. The reweighting factors, called fake factors (FFs), are measured separately for electrons and muons from data in FNP-enriched CRs (CRFF_e and CRFF_μ) as functions of the lepton p_{T} and $|\eta|$. The CRs listed in Table 6 are designed to be as close as possible to the $\text{SR}^{Wh}_{\text{high}-m_{\text{T2}}}$ and $\text{SR}^{Wh}_{\text{low}-m_{\text{T2}}}$ in order to share the same sources of FNP contributions as the target SRs. The measured FFs are around 0.1 for both electrons and muons, reaching up to 0.3 for some p_{T} and $|\eta|$ bins. The uncertainties of this method come principally from the measurement of the FFs which are propagated to the final estimation via the reweighting. In this analysis, the FF uncertainties coming from statistics, possible differences of FNP contributions between the CRs and the targeted SRs, and prompt lepton and CF background subtraction amount to around 20% of the final estimation in total. Two validation regions VRFNP^{Wh} and VRCF^{Wh}, listed in Table 6, are defined to validate the data-driven methods applied for the estimations of FNP and CF events in $\text{SR}^{Wh}_{\text{high}-m_{\text{T2}}}$ and $\text{SR}^{Wh}_{\text{low}-m_{\text{T2}}}$. Good agreement between data and expectation is observed in the VRs, as shown in Figure 3, thus validating the application of the above methods.

The matrix method involves the inversion of the matrix relating the number of observed baseline and signal leptons to the estimated number of real and FNP leptons via measured real (ε) and FNP (ζ) lepton efficiencies; the implementation of Ref. [35] is applied here. The ε is around 50–60% (70%) for electrons (muons) in the region of lepton p_{T} around 15 GeV, increasing up to 98% (99%) for lepton $p_{\text{T}} > 100$ GeV (60 GeV). The total uncertainties for ε vary between 0.33–7% (0.1–3%) for electrons (muons) depending on the (p_{T}, η) region. The ζ probabilities are ~10–20% for both electrons and muons up to $p_{\text{T}} \sim 45$ GeV, and increase to 30–40% for $p_{\text{T}} > 60$ GeV. They can be up to twice as large in events with two b-tagged jets. The variations in the relative contributions of different sources of FNP leptons or in the environment are

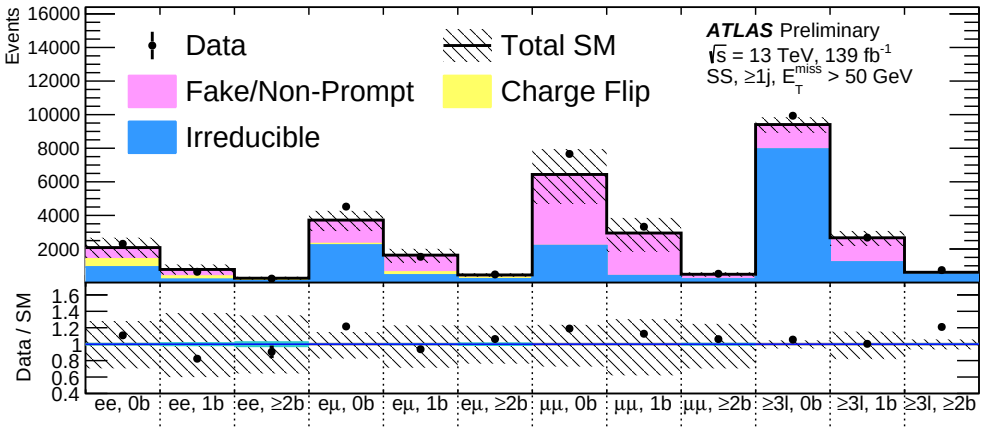

Figure 5: Data event yields compared with the expected contributions from the irreducible and the reducible backgrounds after a loose preselection requiring SS leptons, $E_{\mathrm{T}}^{\mathrm{miss}} > 50\,\mathrm{GeV}$ and at least one jet with $p_{\mathrm{T}} > 25\,\mathrm{GeV}$. The observed and predicted event yields are classified as a function of the number and flavour of the leptons, as well as the number of b-jets. The error bars only include the statistical uncertainty as well as the full uncertainties for the data-driven background estimates. The bottom panel shows the ratio of the observed data to the predicted yields.

considered as uncertainties of ζ. For electrons (muons), the latter is 30–50% (30–80%), increasing with p_{T}. The agreement between the data and the estimated background in a loose event preselection region requiring two SS leptons, $E_{\mathrm{T}}^{\mathrm{miss}} > 50\,\mathrm{GeV}$ and at least one jet with $p_{\mathrm{T}} > 25\,\mathrm{GeV}$, in different lepton-flavour and b-jet-multiplicity combinations, as shown in Figure 5, indicates the universality of the matrix method to estimate the FNP in general cases. Together with the observed agreement in Figure 4, the estimations of the FNP background using the matrix method is validated.

To further validate the estimation of the FNP and the CF backgrounds, the MC template method is introduced to this analysis. It relies on data-corrected CRs enriched in various sources of fake leptons and electron CF backgrounds used to extrapolate the background predictions to the SRs. In this analysis, the correction factors are obtained for seven templates representing different types of backgrounds from six control regions using discriminating variables such as m_{eff} and lepton p_{T}. The uncertainties due to limited statistics and from the effects of the used discriminate variables are considered. The similarity observed in the m_{T2} distributions for SRs defined for the WZ and the bRPV model between the matrix method and the MC template method proves the validity of the background estimation.

8 Systematic uncertainties

In this analysis several sources of systematic uncertainties, besides the various statistical uncertainties, are considered. They are grouped into experimental uncertainties, theoretical uncertainties, uncertainties from the data-driven methods applied in this analysis, normalisation and MC statistical uncertainties.

The experimental uncertainties encompass all possible differences between data and simulations in all analysis elements including trigger, pileup, and reconstructed objects. A 1.7% relative uncertainty on the luminosity [104] is applied to all MC samples that are not normalised in control regions. For leptons, uncertainties on the reconstruction efficiencies [177, 195], identification efficiencies [179], isolation

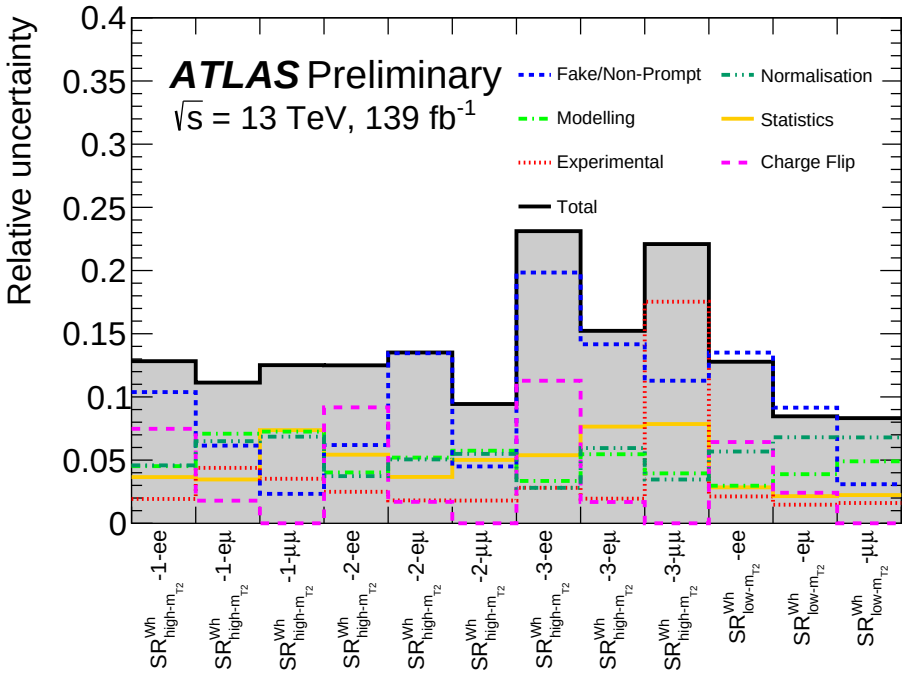

Figure 6: Breakdown of the total systematic uncertainties in the background prediction for the SRs of the Wh model. Total and individual uncertainties for different categories of systematic sources are shown. The individual components can be correlated and therefore do not necessarily add up in quadrature to the total systematic uncertainty.

efficiencies, energy scales [177, 196], resolutions, and trigger efficiencies are considered. For jets, uncertainties for jet vertex tagger [197] which accounts for the residual contamination from pileup jets, uncertainties for jet energy scale [181] and jet energy resolution [198], and uncertainties of flavour tagging [183, 199, 200] are also considered. The uncertainties associated with the objects used to compute the $E_{\mathrm{T}}^{\mathrm{miss}}$ are propagated through the computation, and additional uncertainties in the scale and resolution of the contribution from low-momentum tracks not associated with the primary objects are also included [186]. These experimental uncertainties are correlated between processes and regions that apply the simultaneous fit including the signal models.

The theoretical uncertainties represent the uncertainties in modelling of the relevant SM and SUSY processes including uncertainties on cross sections, choice of scales, the PDF and the α_s. Only dominant background processes for the majority of the signal regions that are defined in this analysis consider the theoretical uncertainties like the WZ, $W^{\pm}W^{\pm}$, and the $t\bar{t}V$ processes. The total cross-section uncertainty is not applied if the background process is normalised to data, but the uncertainties that affect the acceptance such as the choice of the scales and the PDF are applied everywhere. The theoretical uncertainties vary from 10% to 50% in all regions that defined in this analysis. The total uncertainty and the contributions from different sources are shown in Figures 6 and 7 for all the signal regions.

For regions designed for the Wh model, the total uncertainties varied from 5% to 25% which are lower than those SRs designed for the WZ model and the bPRV model due to the estimation of the correlations between the relevant systematics during the fit in the dedicated control regions. The largest contribution is coming from the estimation of the FNP.

For CRs and VRs for the WZ model and the bRPV model, the total uncertainties are less than 1% to 20%

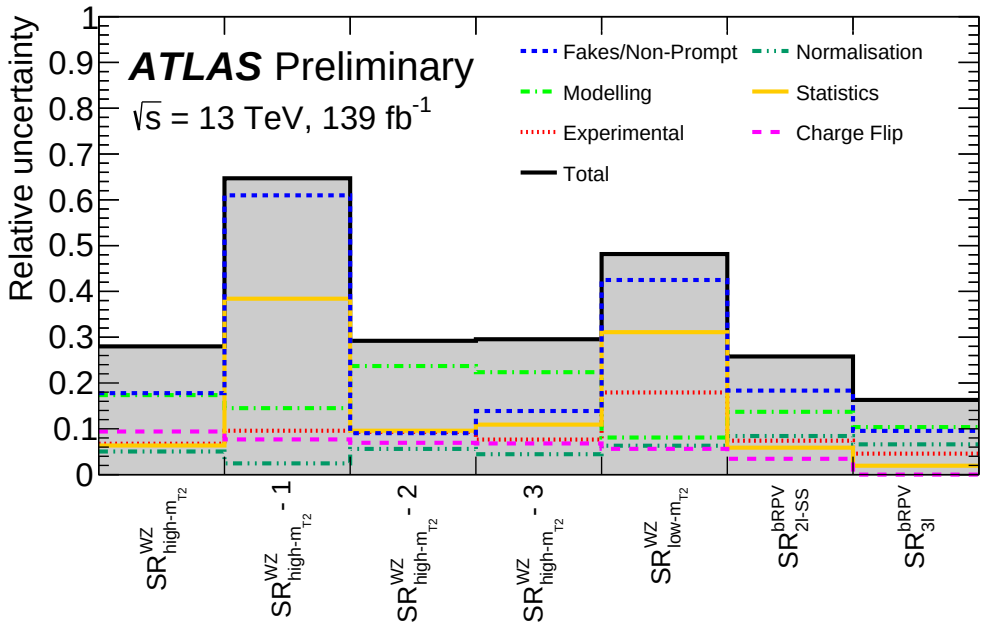

Figure 7: Breakdown of the total systematic uncertainties in the background prediction for the SRs of the WZ and bRPV models. Total and individual uncertainties for different categories of systematic sources are shown. The individual components can be correlated and therefore do not necessarily add up in quadrature to the total systematic uncertainty.

with the largest contribution coming from the modelling of the simulated SM processes. For SRs designed for these two models, total uncertainties vary from 30% to 50% with the uncertainties from the estimations of FNP and CF events accounting for the largest contribution in most of the regions.

9 Results

The $E_{\mathrm{T}}^{\mathrm{miss}}$ and $\mathcal{S}(E_{\mathrm{T}}^{\mathrm{miss}})$ distributions for all events passing the Wh SR requirements, except for the $E_{\mathrm{T}}^{\mathrm{miss}}$ and $\mathcal{S}(E_{\mathrm{T}}^{\mathrm{miss}})$ requirements themselves, are shown in Figure 8 and Figure 9, respectively. Data are compared to the expected SM background; each source estimated as described in Section 7. Separate distributions are provided for each SS-dilepton flavour: $e^{\pm}e^{\pm}$, $e^{\pm}\mu^{\pm}$ and $\mu^{\pm}\mu^{\pm}$. Fake and non-prompt leptons as well as the WZ irreducible background dominate the events mimicking signal events, while the CF events form an important source of background events in the $e^{\pm}e^{\pm}$ SRs, as observed in Figure 8(a) and Figure 9(a). The expected distributions for three representative signal mass points are also overlaid as indicated. Good agreement between the data and total expected SM background is observed.

The observed number of events in each SR defined in Section 6 for the Wh model along with the background expectations and uncertainties are reported in Figure 10. The observed data are compatible with the SM prediction, with a mild -2.02σ data deficit observed in $\mathrm{SR}^{Wh}_{\mathrm{high}-m_{\mathrm{T2}}}$-3-$\mu\mu$.

The distributions of m_{T2} for the SRs defined for the WZ model and the bRPV models after applying all selection criteria apart from the m_{T2} are shown in Figures 11(a) to 11(b) and in Figures 11(c) to 11(d),

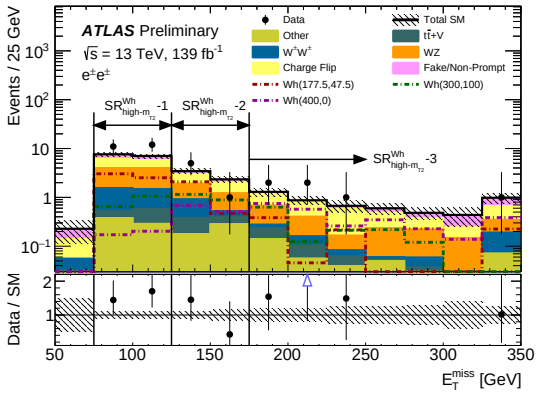

(a) $e^{\pm}e^{\pm}$ channel

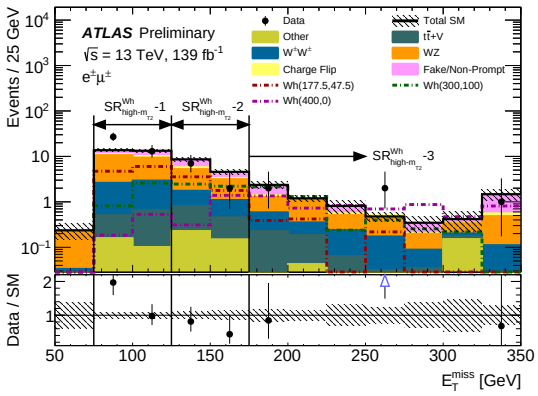

(b) $e^{\pm}\mu^{\pm}$ channel

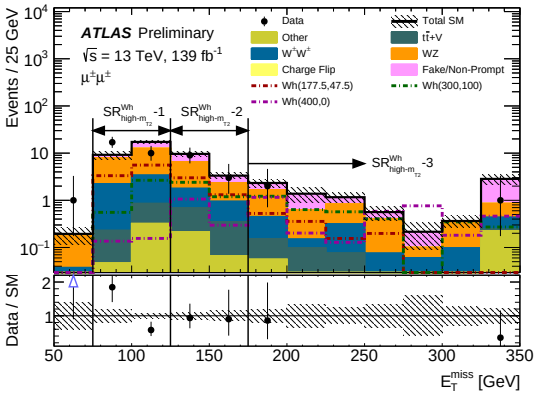

(c) $\mu^{\pm}\mu^{\pm}$ channel

Figure 8: $E_{\mathrm{T}}^{\mathrm{miss}}$ distributions after the background-only fit showing the data and the post-fit expected background, in all the flavour and $E_{\mathrm{T}}^{\mathrm{miss}}$ bins of the $\mathrm{SR}^{Wh}_{\mathrm{high}-m_{\mathrm{T2}}}$ region. The vertical black lines and the corresponding arrows indicate the cuts defining the three $E_{\mathrm{T}}^{\mathrm{miss}}$ bins of the $\mathrm{SR}^{Wh}_{\mathrm{high}-m_{\mathrm{T2}}}$ region: $\mathrm{SR}^{Wh}_{\mathrm{high}-m_{\mathrm{T2}}}$-1, $\mathrm{SR}^{Wh}_{\mathrm{high}-m_{\mathrm{T2}}}$-2, and $\mathrm{SR}^{Wh}_{\mathrm{high}-m_{\mathrm{T2}}}$-3. The last bin includes overflow. The 'Other' category contains the $t\bar{t}+H$, rare top, triboson, and other diboson processes with the SS final state. Distribution for three representative signal mass points of the Wh model are overlaid. The bottom panel shows the ratio of the observed data to the predicted yields. The hatched bands indicate the combined theoretical, experimental, data-driven and MC statistical uncertainties.

respectively. All considered sources of background are also plotted, estimated with the data-driven techniques detailed in Section 7. The background is dominated by the SM WZ process and the reducible background due to fake and non-prompt leptons. The data distributions are in agreement with the background expectations.

In Figure 12, the observed yields in each signal region defined in Section 6 along with the background expectations and uncertainties are presented for the WZ and bRPV models. The observed data are compatible with the SM prediction, thus allowing to set limits on the parameters of these theoretical scenarios.

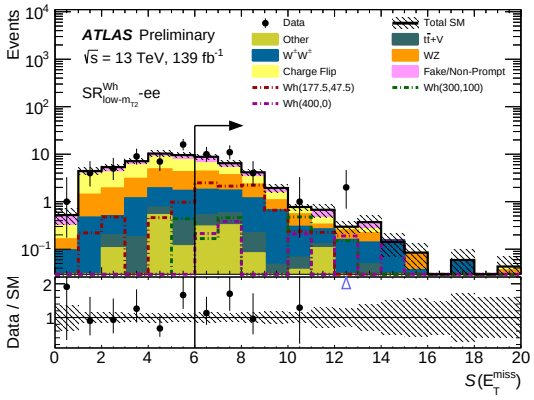

(a) $e^{\pm}e^{\pm}$ channel

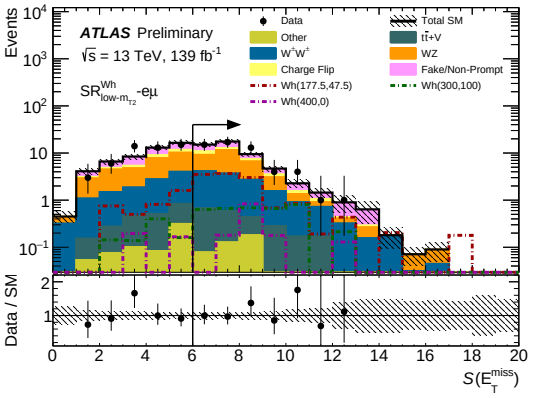

(b) $e^{\pm}\mu^{\pm}$ channel

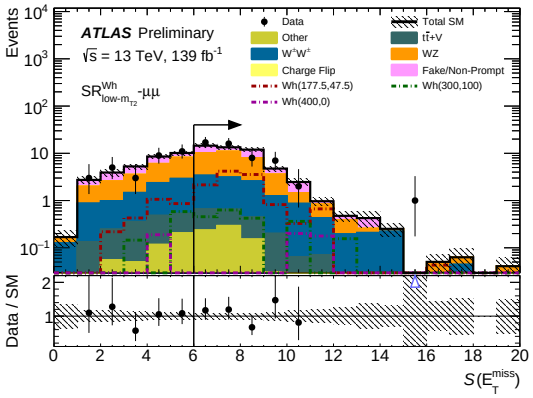

(c) $\mu^{\pm}\mu^{\pm}$ channel

Figure 9: $\mathcal{S}(E_{\mathrm{T}}^{\mathrm{miss}})$ distributions after the background-only fit showing the data and the post-fit expected background, in all the flavour bins of the $\mathrm{SR}^{Wh}_{\mathrm{low}-m_{\mathrm{T2}}}$ region. The vertical black line and the corresponding arrow indicates the cut defining the $\mathrm{SR}^{Wh}_{\mathrm{low}-m_{\mathrm{T2}}}$ region. The last bin includes overflow. The 'Other' category contains the $t\bar{t}+H$, rare top, triboson, and other diboson processes with the SS final state. Distribution for three representative signal mass points of the Wh model are overlaid. The bottom panel shows the ratio of the observed data to the predicted yields. The hatched bands indicate the combined theoretical, experimental, data-driven and MC statistical uncertainties.

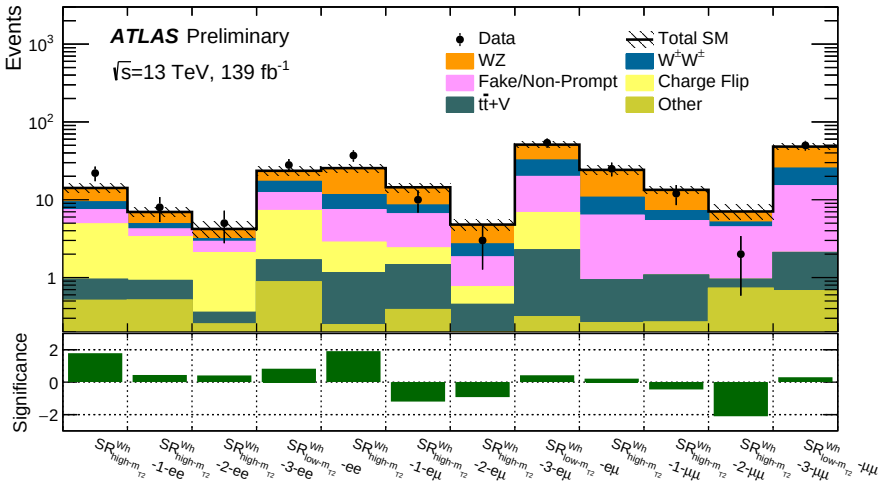

Figure 10: Expected SM background and data yields in the SRs optimised for the Wh model. The total uncertainties in the expected event yields are shown as the hashed bands. The SM prediction is taken from the background-only fit. The 'Other' category contains the $t\bar{t}$+H, rare top, triboson, and other diboson processes with the SS final state. The bottom panel shows the statistical significance [191] of the discrepancy between the observed number of events and the SM expectation.

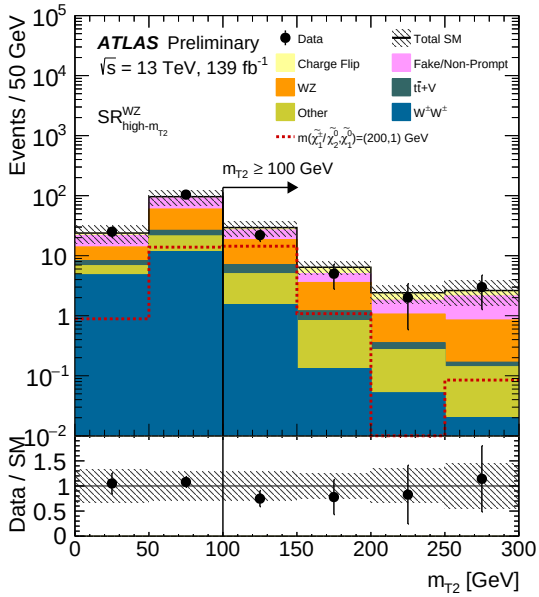

(a) $\mathrm{SR}^{WZ}_{\mathrm{high}-m_{\mathrm{T2}}}$

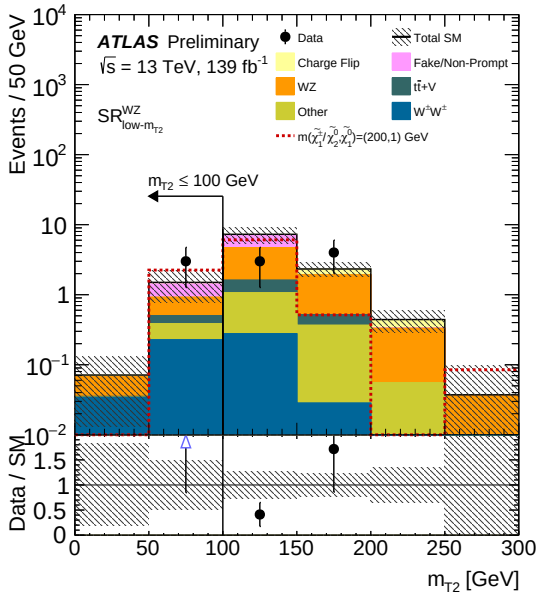

(b) $\mathrm{SR}^{WZ}_{\mathrm{low}-m_{\mathrm{T2}}}$

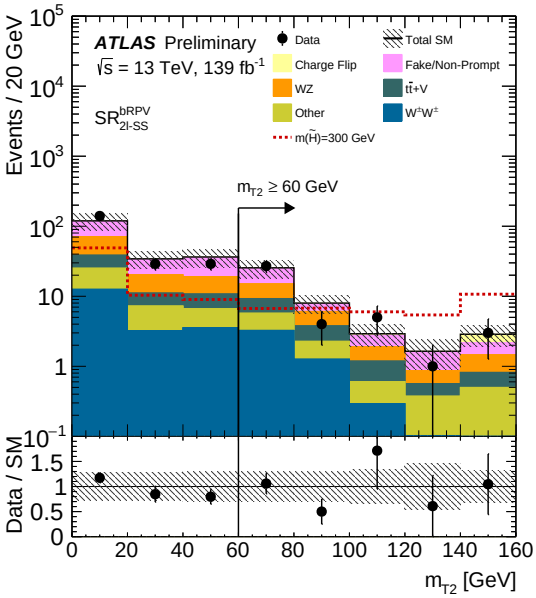

(c) $\mathrm{SR}^{\mathrm{bRPV}}_{2\ell-\mathrm{SS}}$

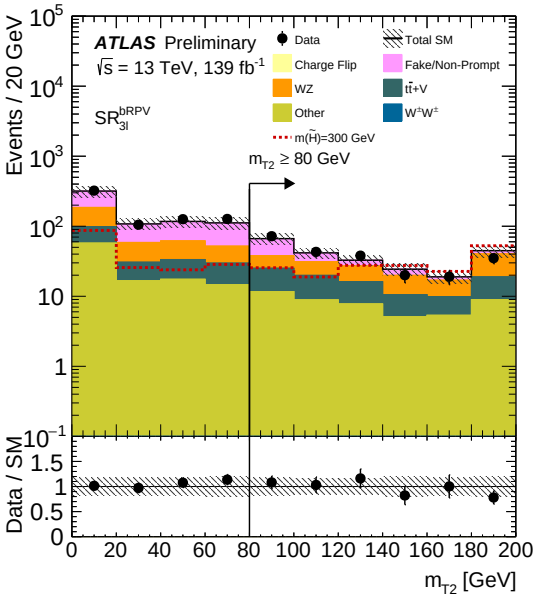

(d) $\mathrm{SR}^{\mathrm{bRPV}}_{3\ell}$

Figure 11: m_{T2} distributions for SRs defined for the WZ model ((a) and (b)) and the bRPV model ((c) and (d)). All SR selection criteria are satisfied except for that on m_{T2}. The vertical black lines and the corresponding arrows indicate the corresponding cuts defining those regions. The matrix method is used for background estimation and the CF events are estimated via a data-driven method. The 'Other' category contains the $t\bar{t}+H$, rare top, triboson, and other diboson processes with the SS final state. Uncertainties from theoretical, experimental, data-driven and MC statistics are all considered. The last bin includes overflow. The bottom panel shows the ratio of the observed data to the predicted yields.

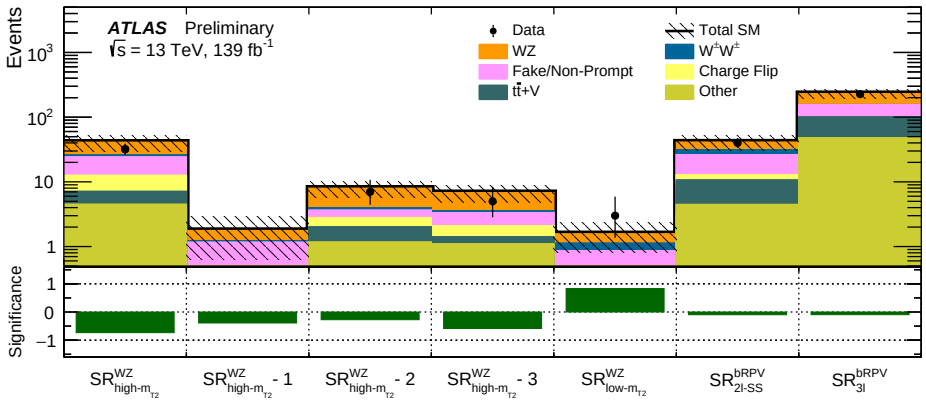

Figure 12: Expected SM background and data yields in the SRs optimised for the WZ and bRPV model. The SM prediction is taken from the background-only fit. The 'Other' category contains the $t\bar{t}+H$, rare top, triboson, and other diboson processes with the SS final state. The total uncertainties in the expected event yields are shown as the hashed bands. The bottom panel shows the statistical significance [191] of the discrepancy between the observed number of events and the SM expectation.

10 Interpretation

Model-independent upper limits on the number of BSM events for each SR are derived using the CL_s prescription [201, 202] and neglecting any possible contamination in the control regions. The HistFitter [190] framework is used for the statistical interpretation of the results. In order to quantify the probability for the background-only hypothesis to fluctuate to the observed number of events or higher, a one-sided p_0-value is calculated using pseudo-experiments, where the profile likelihood ratio is used as a test statistic [189] to exclude the signal-plus-background hypothesis. Normalisation to the integrated luminosity of the data sample allows the interpretation in terms of upper limits on the visible BSM cross section, defined as the product of acceptance, reconstruction efficiency and production cross-section.

The number of observed events and the background expectation in each SR are used to set an upper limit on the number of events from any BSM physics scenario. The model-independent upper limits at 95% confidence level (CL) on the visible cross section, $\langle \epsilon\sigma \rangle^{95}_{\text{obs}}$, for the the Wh, WZ and bRPV models are presented in Table 7. Also listed are the 95% CL upper limits on the number of signal events S^{95}_{obs}, as well as the expected 95% CL upper limit on the number of signal events, S^{95}_{exp}. The last two columns indicate the CL_b value and the discovery p-value, p_0 ($p(s) = 0$), with the corresponding gaussian significance Z. The CL_b provides a measure of compatibility of the observed data with the 95% CL signal strength hypothesis relative to fluctuations of the background, and p_0 measures the compatibility of the observed data with the background-only (zero signal strength) hypothesis relative to fluctuations of the background. Larger values indicate greater relative compatibility.

For $\text{SR}^{WZ}_{\text{high}-m_{\text{T2}}}$, $\text{SR}^{\text{bRPV}}_{2\ell-\text{SS}}$ and $\text{SR}^{\text{bRPV}}_{3\ell}$, p_0 is capped at 0.5, since the predictions exceed the data. In all other SRs the significances are low, with no excess over the background being observed. The most stringent observed limit is from $\text{SR}^{WZ}_{\text{low}-m_{\text{T2}}}$, where visible cross sections larger than 0.04 fb are excluded; the same limit is obtained in some *UDD* RPV SRs in Table 9.

Table 7: Model-independent statistical analysis for SRs optimised for the Wh, WZ and bRPV models: 95% CL upper limits on the visible cross section, $\langle \epsilon\sigma \rangle^{95}_{\text{obs}}$, and on the number of signal events S^{95}_{obs}. The S^{95}_{exp} is the expected 95% CL upper limit on the number of signal events, given the the expectation (and $\pm 1\sigma$ variations) of background events. The last two columns report the CL_b value for the background-only hypothesis, the one-sided p_0-value and the local significance Z (the number of equivalent Gaussian standard deviations).

Signal channel	$\langle \epsilon\sigma \rangle^{95}_{\text{obs}}$ [fb]	S^{95}_{obs}	S^{95}_{exp}	CL_b	p_0 (Z)
$\text{SR}^{Wh}_{\text{high}-m_{\text{T2}}}$	0.28	39.3	$33.9^{+14.3}_{-10.0}$	0.66	0.34 (0.41)
$\text{SR}^{Wh}_{\text{low}-m_{\text{T2}}}$	0.24	33.0	$29.5^{+11.7}_{-8.8}$	0.63	0.33 (0.43)
$\text{SR}^{WZ}_{\text{high}-m_{\text{T2}}}$	0.13	18.7	$24.4^{+6.8}_{-5.0}$	0.12	0.50 (0.00)
$\text{SR}^{WZ}_{\text{low}-m_{\text{T2}}}$	0.04	5.9	$4.4^{+1.8}_{-0.8}$	0.81	0.22 (0.76)
$\text{SR}^{\text{bRPV}}_{2\ell-\text{SS}}$	0.16	22.6	$25.8^{+7.9}_{-5.8}$	0.29	0.50 (0.00)
$\text{SR}^{\text{bRPV}}_{3\ell}$	0.44	61.4	$93.0^{+56.0}_{-20.3}$	0.02	0.50 (0.00)

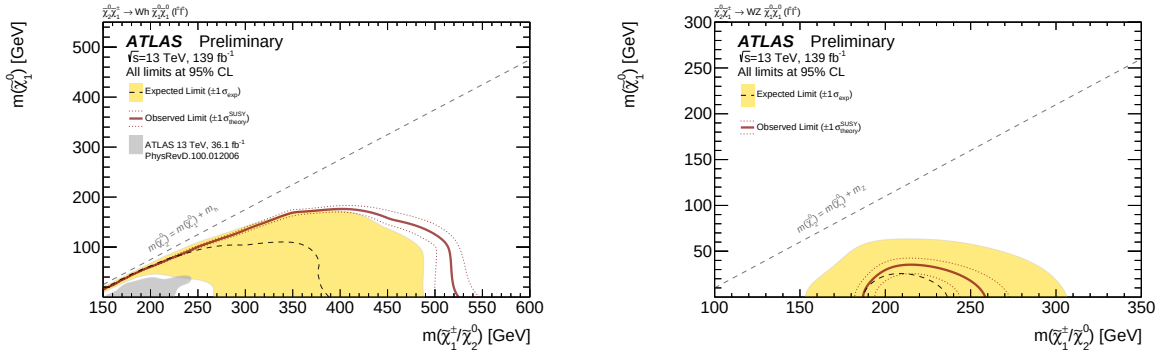

(a) Wino $\tilde{\chi}_1^{\pm}\tilde{\chi}_2^0$ with Wh

(b) Wino $\tilde{\chi}_1^{\pm}\tilde{\chi}_2^0$ with WZ

Figure 13: Exclusion limits at 95% CL for the (a) Wh-mediated and the (b) WZ-mediated simplified model of wino $\tilde{\chi}_1^{\pm}\tilde{\chi}_2^0$ production. Observed (solid) and expected (dashed) limits on $\tilde{\chi}_1^{\pm}/\tilde{\chi}_2^0$ and $\tilde{\chi}_1^0$ masses. The red dotted lines around the observed limit reflect the theoretical variation due to the signal cross-section uncertainty. The band around the expected limits express the $\pm 1\sigma$ variation due to all uncertainties except theoretical uncertainties in the signal cross-section. The grey region in (a) denotes the observed limits obtained in a previous search in the same channel with 36.1 fb^{-1} of data [43].

Model-dependent exclusion limits have been extracted by performing a statistical interpretation of the results also using the HistFitter package. The procedure to extract the limits is a model-dependent fit, which performs hypothesis tests on the background-only hypothesis and the signal-plus-background hypothesis. Both of the fits have been carried out simultaneously in all SRs designed for each model and for each assumed benchmark point. The signal contribution to each region participating in the fit is taken into account together with its uncertainty according to the model predictions. Following the CL_s prescription, the p-values of the signal-plus-background hypothesis are tested against those of the background-only hypothesis to extract the corresponding CL_s values for each point. A signal point is considered excluded at 95% CL when such values fall below the 5% threshold.

The resulting expected and observed exclusion limit for the Wh model is shown in Figure 13(a). All SRs are statistically combined. The large $\pm 1\sigma$ uncertainty band of the expected limit, shown in Figure 13(a), is almost entirely dominated by the statistical error on the signals from MC. The observed bounds are stronger than the expected ones due to the deficit of data with respect to the SM background expectation seen in $\mathrm{SR}^{Wh}_{\mathrm{high}-m_{\mathrm{T2}}}$-3-$\mu\mu$, as shown in Figure 10. However, this discrepancy falls within the 2σ fluctuation of the expected limit.

In the Wh model, $\tilde{\chi}_1^{\pm}$ $\tilde{\chi}_2^0$ masses are excluded up to about 525 GeV for a massless $\tilde{\chi}_1^0$. On the other hand, the exclusion for $\tilde{\chi}_1^0$ masses reaches about 180 GeV for $m(\tilde{\chi}_1^{\pm}\tilde{\chi}_2^0) \simeq 400$ GeV. The comparison with the observed exclusion limits of the previous 36.1 fb^{-1} search [43] in the same channel, demonstrates the large improvement of the reach of the current analysis.

The observed and expected exclusion limits for the WZ model are shown in Figure 13(b), where two orthogonal SRs, $\mathrm{SR}^{WZ}_{\mathrm{high}-m_{\mathrm{T2}}}$ and $\mathrm{SR}^{WZ}_{\mathrm{low}-m_{\mathrm{T2}}}$, are statistically combined. The deficit of data events compared to the SM expectation in $\mathrm{SR}^{WZ}_{\mathrm{high}-m_{\mathrm{T2}}}$ leads to the observed limits being more stringent than the expected ones, as seen in Figure 12, yet within the 1σ band of the latter. The uncertainty on the expected exclusion limit is dominated by the FNP background determination, as observed in Figure 7. For $m(\tilde{\chi}_1^0) < 1$ GeV,

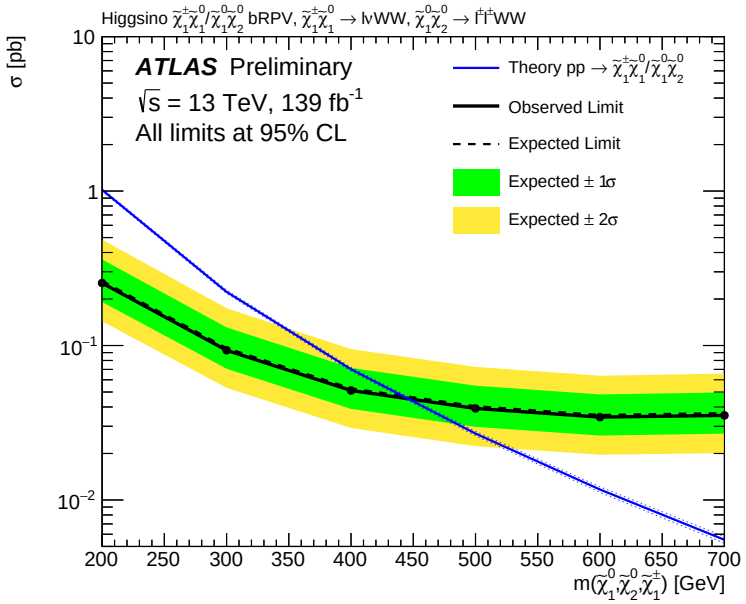

Figure 14: Observed (black solid line) and expected (black dashed line) 95% CL exclusion limits as a function of higgsino $\tilde{\chi}_1^0/\tilde{\chi}_2^0/\tilde{\chi}_1^{\pm}$ mass in the bilinear RPV model. The green (yellow) contours of the band around the expected limit are the $\pm 1\sigma$ ($\pm 2\sigma$) variations including all uncertainties. The prediction for the theoretical production cross-section is also shown (blue solid line) with its uncertainty (blue dotted lines).

$\tilde{\chi}_1^{\pm}/\tilde{\chi}_2^0$ masses in the interval 190–250 GeVare excluded. This is the first analysis in ATLAS with sensitivity to the WZ model in the two SS lepton channel.

The expected and observed production cross-section upper limits for light higgsinos in the bRPV model can be seen in Figure 14 with the statistical combination of two orthogonal SRs, namely $\mathrm{SR}^{\mathrm{bRPV}}_{2\ell-\mathrm{SS}}$ and $\mathrm{SR}^{\mathrm{bRPV}}_{3\ell}$. By comparing the observed upper cross-section limits with the theoretical expected cross section, higgsino $\tilde{\chi}_1^0/\tilde{\chi}_2^0/\tilde{\chi}_1^{\pm}$ masses smaller than 440 GeV are excluded assuming an inclusive higgsino production and allowing all predicted sparticle decay modes. These are the first experimental constraints on bRPV models with degenerate higgsino masses.

11 Conclusion

This paper presents a search for directly produced electroweak gauginos and higgsinos in events with two electrons or muons of the same charge or three leptons based on a 139 fb^{-1} sample of $\sqrt{s}$ = 13 TeV proton–proton collisions collected by the ATLAS experiment at the LHC from 2015 to 2018. Events are categorised according to the number of jets, b-jets, the missing transverse momentum, the effective mass and other relevant observables, improving substantially the sensitivity to specific R-parity-conserving and R-parity-violating scenarios. No significant excess over the expected background is observed. Observed 95% CL limits on the visible cross-section are placed in the defined signal regions and constraints have been set on the parameters of the simplified topologies and complete models considered. In a wino-bino Wh-mediated model, NLSP masses of up to 525 GeV have been excluded for a massless lightest neutralino, extending considerably previous limits set by ATLAS [43] with a 36.1 fb^{-1} dataset and CMS [46] with a

137 fb^{-1} sample of 240 GeVand 300 GeV, respectively. The analogous excluded $\tilde{\chi}_1^{\pm}/\tilde{\chi}_2^0$ mass range for the WZ topology is between 190 GeVand 260 GeVin a channel probed for the first time in ATLAS. In a natural RPV model with bilinear terms, never explored before in electroweak SUSY production, mass-degenerate higgsinos $\tilde{\chi}_1^0/\tilde{\chi}_2^0/\tilde{\chi}_1^{\pm}$ lighter than 440 GeV have been excluded. Model-independent production cross-section upper bounds as low as 40 ab have been set in signal regions inspired by an R-parity-breaking scenario with a baryon-number violating term. Search regions orthogonal to other ATLAS analyses have been deployed in all considered models, simplifying future statistical combinations with other channels.

Appendix

A RPV analysis with *UDD* terms

A.1 Signal regions

The signal regions designed to maximise the signal sensitivities of this grid are listed in Table 8. Orthogonal signal regions are defined with the number of b-jets. In each case, signal regions are further split according to the jet multiplicity targeting different higgsino mass ranges.

Within each SR, variables like the sum of the jets p_{T} ($\sum p_{\mathrm{T}}^{\mathrm{jet}}$), the fraction of the sum of the b-jets p_{T} among the sum of jets p_{T} ($\sum p_{\mathrm{T}}^{b\text{-jet}} / \sum p_{\mathrm{T}}^{\mathrm{jet}}$), the minimum angular distance between the leading lepton and jets ($\Delta R(\ell_1, \mathrm{jet})_{\mathrm{min}}$) and the angular distance between the two SS pair leptons are used to maximise the sensitivity to the target signal based on a series of dedicated optimisation studies.

Table 8: Signal region definitions designed for the *UDD* RPV model. The variables are defined in the text.

	$\mathrm{SR}^{\mathrm{RPV}}_{2\ell 1b}$		$\mathrm{SR}^{\mathrm{RPV}}_{2\ell 2b}$			$\mathrm{SR}^{\mathrm{RPV}}_{2\ell 3b}$		
	L	M	L	M	H	L	M	H
$N_{\mathrm{BL}}(\ell)$	= 2							
$N_{\mathrm{Sig}}(\ell)$	= 2							
Charge(ℓ)	same-sign							
$p_{\mathrm{T}}(\ell)$	> 25 GeV							
n_{jets} (p_{T} > 25 GeV)	≥ 1							
$n_{b\text{-jets}}$	= 1		= 2			= 3		
$\sum p_{\mathrm{T}}(\ell)$	≥ 100 GeV		–			–		
$E_{\mathrm{T}}^{\mathrm{miss}}$	≥ 100 GeV	≥ 50 GeV	≥ 80 GeV			≥ 20 GeV		
n_{jets} (p_{T} > 25 GeV)	≤ 2	= 2 or = 3	≤ 3	=3 or = 4	≥ 5 and ≤ 6	≤ 3	≤ 3	≤ 6
$\sum p_{\mathrm{T}}^{b\text{-jet}} / \sum p_{\mathrm{T}}^{\mathrm{jet}}$	≥ 0.7	≥ 0.45	≥ 0.9	≥ 0.75	–	≥ 0.8	≥ 0.8	≥ 0.5
$\sum p_{\mathrm{T}}^{\mathrm{jet}}$	≥ 120 GeV	≥ 400 GeV	≥ 300 GeV	≥ 420 GeV	≥ 420 GeV	–	–	≥ 350 GeV
$\Delta R(\ell_1, \mathrm{jet})_{\mathrm{min}}$	≤ 1.2	≤ 1.0	≤ 1.0	≤ 1.0	≤ 1.0	≤ 1.5	–	≤ 1.0
$\Delta R(\ell^{\pm}, \ell^{\pm})$	≥ 2.0	≥ 2.5	≥ 2.5	≥ 2.5	≥ 2.0	≥ 2.0	–	≥ 2.0

A.2 Background estimation and systematic uncertainties

The background composition is similar to the SRs described in Section 6 but with $t\bar{t}$+V as the dominant irreducible background in the above SRs due to the b-jet-requiring.

The background estimation strategy is the same as the one used for those regions designed for the WZ and bRPV models, described in detail in Section 7. The irreducible backgrounds are estimated through MC simulation, after applying data-driven correction factors for the WZ background events with at least two jets obtained from $\mathrm{CR}WZ_{2j}^{WZ,(\mathrm{b})\mathrm{RPV}}$. The CF events are estimated via the data-driven method described in Section 7. The FNP events are estimated from the data by applying the matrix method, after being validated by comparing the estimations with the MC template method.

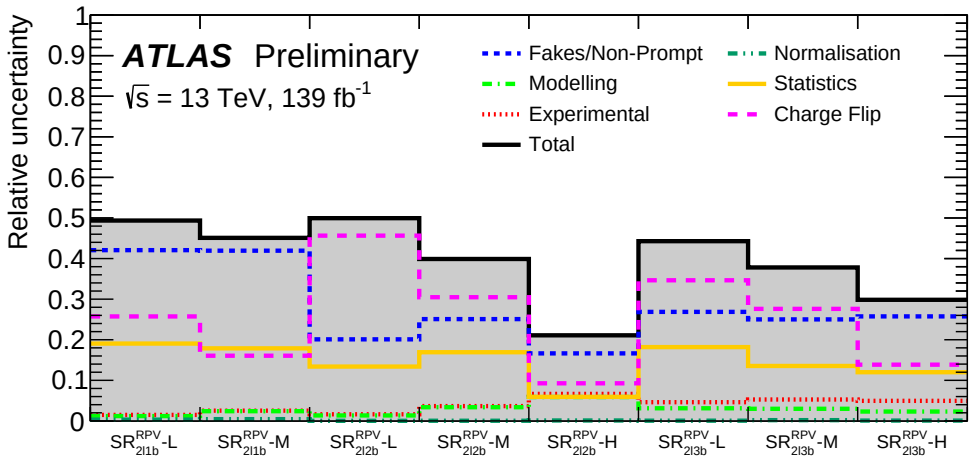

Figure 15: Relative contributions from experimental and theoretical uncertainties in SRs defined for the *UDD* RPV model. The individual components can be correlated and therefore do not necessarily add up in quadrature to the total systematic uncertainty.

Figure 15 shows the uncertainties contributions in the signal regions designed for this model. The uncertainties varies from 20% to 50% depending on the regions. The largest contribution is coming from the data-driven methods applied.

A.3 Results

The $\sum p_{\mathrm{T}}^{b\text{-jet}} / \sum p_{\mathrm{T}}^{\mathrm{jet}}$ distributions in a subset of SRs for the data and background sources are presented in Figure 16. All selection criteria defined in Table 8 are applied apart from the one on $\sum p_{\mathrm{T}}^{b\text{-jet}} / \sum p_{\mathrm{T}}^{\mathrm{jet}}$, which is also indicated in the graphs by a vertical line and an arrow. Data and total background expectation are in agreement, considering the involved uncertainties.

The comparison between data and background yields for all the SRs defined for the *UDD* RPV model is shown in Figure 17. Observed and expected number of events are compatible in all SRs, with the largest excess, observed in $\mathrm{SR}^{\mathrm{RPV}}_{2\ell 3b}$-H. These results are used to set model-independent upper limits on BSM production cross sections as low as 40 ab, following the procedure described in Section 10, which are listed in Table 9.

Figure 18 shows the expected upper limits of higgsino *UDD* RPV model. All combinations of orthogonal SRs which targeted at same mass points are considered, including $\mathrm{SR}^{\mathrm{RPV}}$-L (the statistical combination of $\mathrm{SR}^{\mathrm{RPV}}_{2\ell 1b}$-L, $\mathrm{SR}^{\mathrm{RPV}}_{2\ell 2b}$-L, $\mathrm{SR}^{\mathrm{RPV}}_{2\ell 3b}$-L), $\mathrm{SR}^{\mathrm{RPV}}$-M (the statistical combination of $\mathrm{SR}^{\mathrm{RPV}}_{2\ell 1b}$-M, $\mathrm{SR}^{\mathrm{RPV}}_{2\ell 2b}$-M, $\mathrm{SR}^{\mathrm{RPV}}_{2\ell 3b}$-M) and $\mathrm{SR}^{\mathrm{RPV}}$-H (the statistical combination of $\mathrm{SR}^{\mathrm{RPV}}_{2\ell 2b}$-H, $\mathrm{SR}^{\mathrm{RPV}}_{2\ell 3b}$-H). Among these combinations, the one providing the expected strongest limit is chosen for each $\tilde{\chi}^0_{1,2}$ mass point.

A higgsino-like $\tilde{\chi}^0_1/\tilde{\chi}^0_2$ mass of 200 GeV is excluded in this analysis considering $\tilde{\chi}^0_1\tilde{\chi}^0_2$ production only. This value has been excluded by an ATLAS search [83] based on the selection of events with one lepton, however using in addition $\tilde{\chi}^\pm_1\tilde{\chi}^0_1$ and $\tilde{\chi}^\pm_1\tilde{\chi}^0_2$ production with $\tilde{\chi}^\pm_1 \to bbs$.

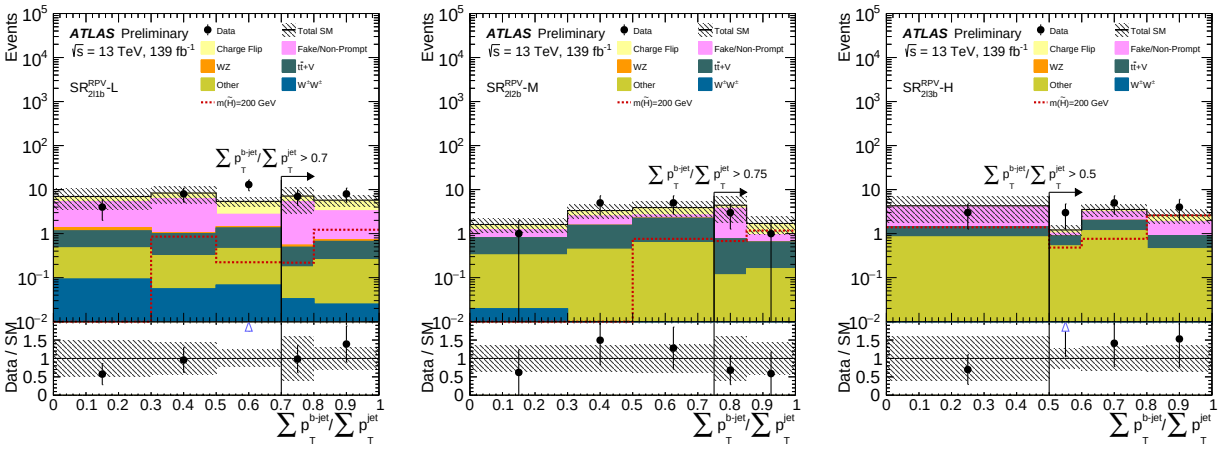

(a) $\mathrm{SR}^{\mathrm{RPV}}_{2\ell 1b}$-L (b) $\mathrm{SR}^{\mathrm{RPV}}_{2\ell 2b}$-M (c) $\mathrm{SR}^{\mathrm{RPV}}_{2\ell 3b}$-H

Figure 16: $\sum p_{\mathrm{T}}^{b\text{-jet}} / \sum p_{\mathrm{T}}^{\mathrm{jet}}$ distributions of the data and the expected background for some SRs defined for the *UDD* RPV model with data-driven methods applied. All uncertainties are considered. The vertical black lines and the corresponding arrows indicate the corresponding cuts defining those regions. The last bin includes overflow. The 'Other' category contains the $t\bar{t}+H$, rare top, triboson, and other diboson processes with the SS final state. The bottom panel shows the ratio of the observed data to the predicted yields.

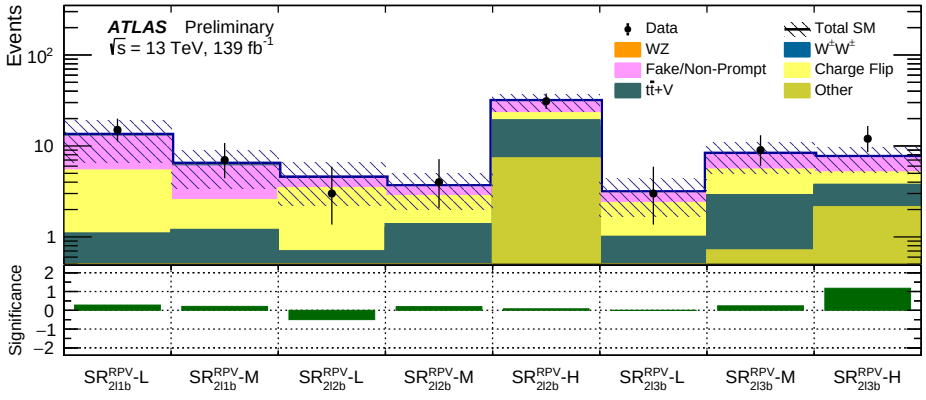

Figure 17: Expected SM background and data yields in the SRs optimised for the *UDD* RPV model. The SM prediction is taken from the background-only fit. The 'Other' category contains the $t\bar{t}+H$, rare top, triboson, and other diboson processes with the SS final state. The total uncertainties in the expected event yields are shown as the hashed bands. The bottom panel shows the statistical significance [191] of the discrepancy between the observed number of events and the SM expectation.

Table 9: Model-independent statistical analysis for SRs optimised for the *UDD* RPV models: the 95% CL upper limit on the visible cross section times efficiency ($\langle\epsilon\sigma\rangle^{95}_{\text{obs}}$), the observed number of signal events (S^{95}_{obs}), and the signal events given the expected number of background events (S^{95}_{exp}, $\pm1\sigma$ variations of the expected number). The last two columns report the CL_b value for the background-only hypothesis, the one-sided p_0-value and the local significance Z (the number of equivalent Gaussian standard deviations).

Signal channel	$\langle\epsilon\sigma\rangle^{95}_{\text{obs}}$ [fb]	S^{95}_{obs}	S^{95}_{exp}	CL_b	p_0 (Z)
$\text{SR}^{\text{RPV}}_{2\ell 1b}$-L	0.13	17.5	$15.1^{+4.8}_{-3.7}$	0.69	0.38 (0.32)
$\text{SR}^{\text{RPV}}_{2\ell 1b}$-M	0.07	10.1	$8.9^{+3.1}_{-1.7}$	0.66	0.46 (0.11)
$\text{SR}^{\text{RPV}}_{2\ell 2b}$-L	0.04	6.1	$6.2^{+2.4}_{-1.1}$	0.48	0.50 (0.00)
$\text{SR}^{\text{RPV}}_{2\ell 2b}$-M	0.05	6.8	$6.0^{+2.3}_{-1.2}$	0.65	0.38 (0.30)
$\text{SR}^{\text{RPV}}_{2\ell 2b}$-H	0.15	20.7	$18.6^{+6.0}_{-4.3}$	0.64	0.41 (0.22)
$\text{SR}^{\text{RPV}}_{2\ell 3b}$-L	0.04	6.1	$5.7^{+1.9}_{-1.0}$	0.61	0.50 (0.00)
$\text{SR}^{\text{RPV}}_{2\ell 3b}$-M	0.08	11.5	$9.7^{+3.2}_{-1.8}$	0.70	0.35 (0.37)
$\text{SR}^{\text{RPV}}_{2\ell 3b}$-H	0.10	13.5	$8.6^{+3.2}_{-2.5}$	0.92	0.10 (1.31)

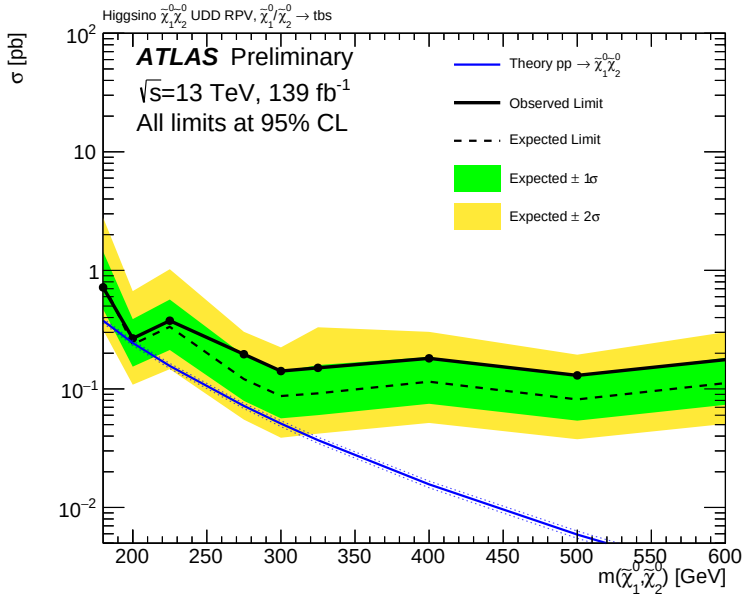

Figure 18: Observed (black solid line) and expected (black dashed line) 95% CL exclusion limits as a function of higgsino $\tilde{\chi}_1^0/\tilde{\chi}_2^0$ mass in the *UDD* RPV model. The green (yellow) contours of the band around the expected limit are the $\pm1\sigma$ ($\pm2\sigma$) variations including all uncertainties. The prediction for the theoretical production cross-section is also shown (blue solid line) with its uncertainty (blue dotted lines).

B Auxiliary material

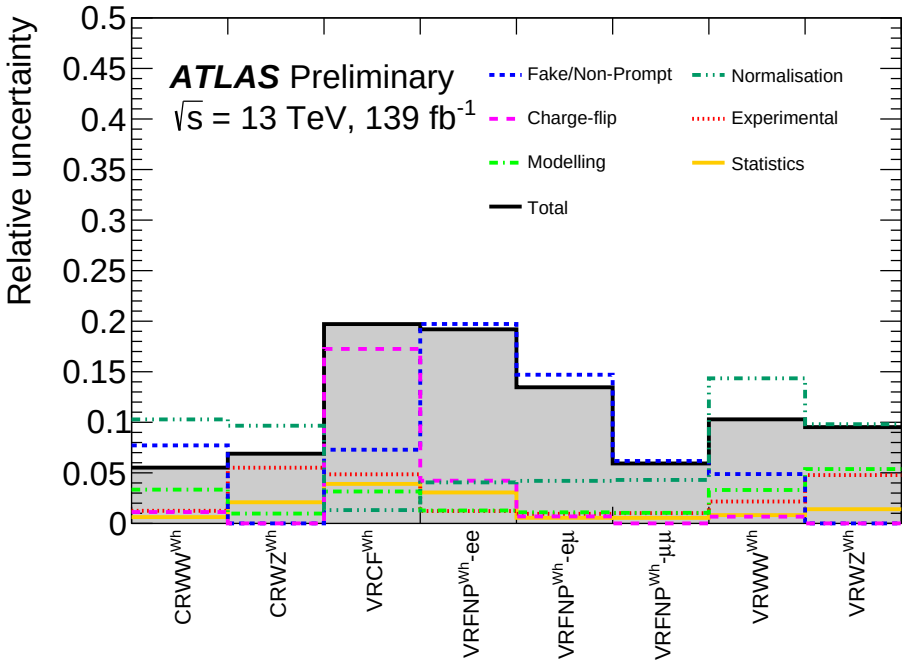

Figure 19: Breakdown of the total post-fit systematic uncertainties in the background prediction for the CRs and VRs of the Wh model. Total and individual uncertainties for different categories of systematic sources are shown. The individual components can be correlated and therefore do not necessarily add up in quadrature to the total systematic uncertainty.

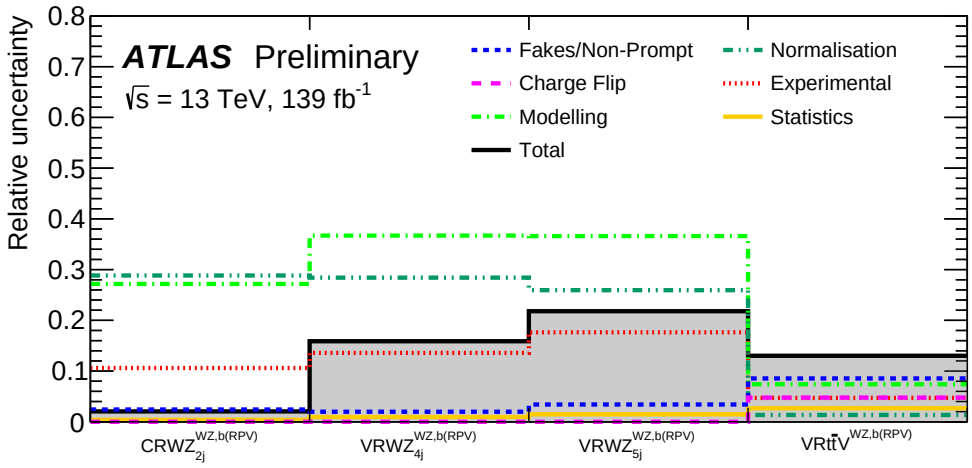

Figure 20: Breakdown of the total post-fit systematic uncertainties in the background prediction for the CRs and VRs of the WZ and bRPV models. Total and individual uncertainties for different categories of systematic sources are shown. The individual components can be correlated and therefore do not necessarily add up in quadrature to the total systematic uncertainty.

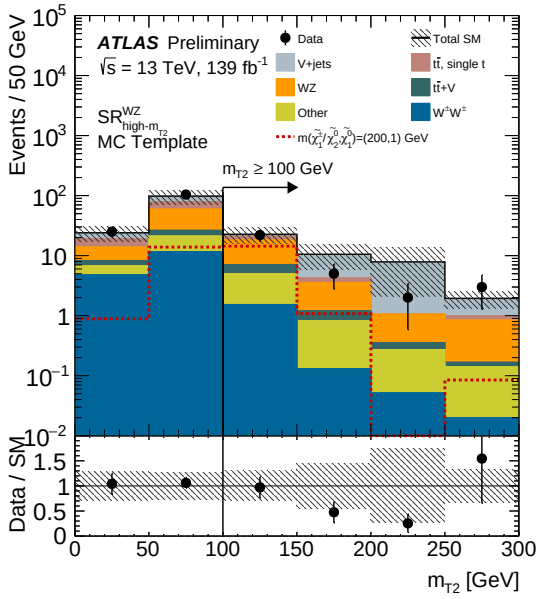

(a) $\mathrm{SR}^{WZ}_{\mathrm{high}-m_{\mathrm{T2}}}$

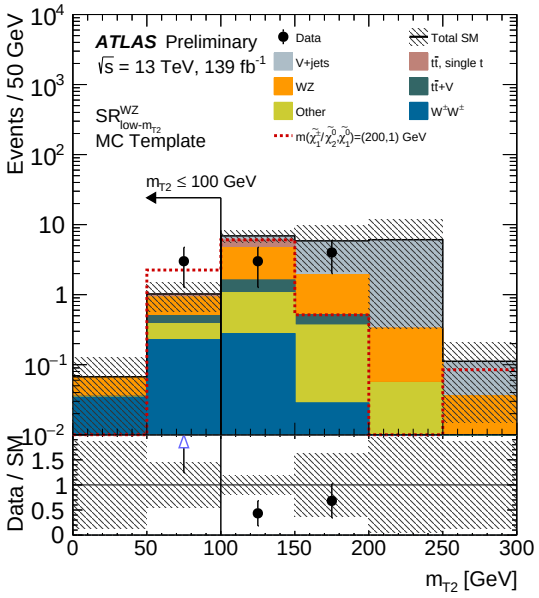

(b) $\mathrm{SR}^{WZ}_{\mathrm{low}-m_{\mathrm{T2}}}$

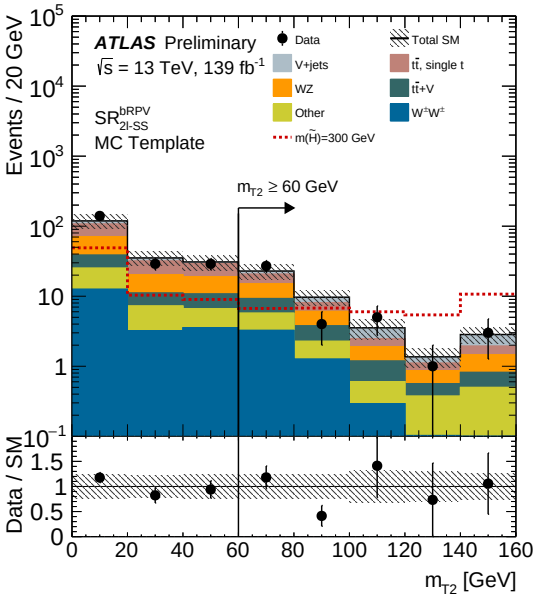

(c) $\mathrm{SR}^{\mathrm{bRPV}}_{2\ell-\mathrm{SS}}$

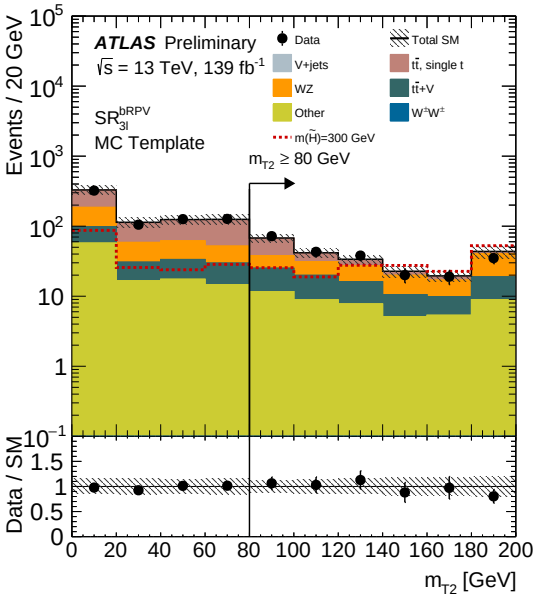

(d) $\mathrm{SR}^{\mathrm{bRPV}}_{3\ell}$

Figure 21: Distributions of m_{T2} for SRs defined for the WZ model ((a) and (b)) and the bRPV model ((c) and (d)). All SR selection criteria are satisfied except for that on m_{T2}. The vertical black lines and the corresponding arrows indicate the corresponding cuts defining those regions. The MC template method is applied for the background estimation. The 'Other' category contains the rare top, triboson, and other diboson processes with the SS final state. Uncertainties from theoretical, experimental, data-driven and MC statistics are all considered. The last bin includes overflow. The bottom panel shows the ratio of the observed data to the predicted yields.

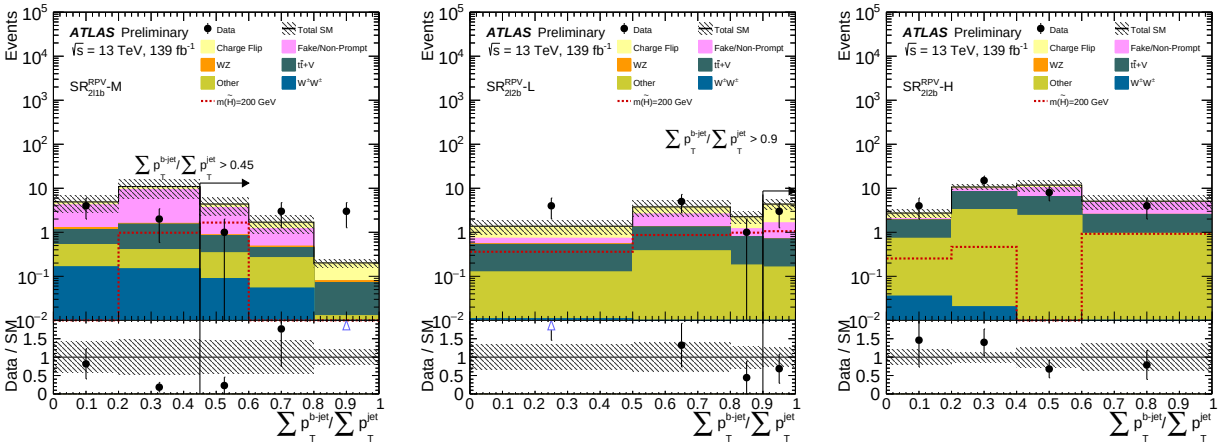

(a) $\mathrm{SR}^{\mathrm{RPV}}_{2\ell 1b}$-M (b) $\mathrm{SR}^{\mathrm{RPV}}_{2\ell 2b}$-L (c) $\mathrm{SR}^{\mathrm{RPV}}_{2\ell 2b}$-H

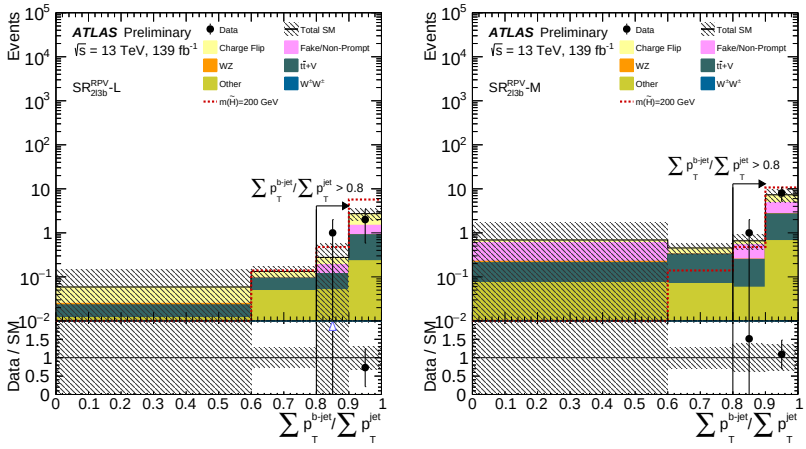

(d) $\mathrm{SR}^{\mathrm{RPV}}_{2\ell 3b}$-L (e) $\mathrm{SR}^{\mathrm{RPV}}_{2\ell 3b}$-M

Figure 22: $\sum p_{\mathrm{T}}^{b\text{-jet}}/\sum p_{\mathrm{T}}^{\mathrm{jet}}$ distributions of the data and the expected background for SRs defined for the *UDD* RPV model with data-driven methods applied. All SR selection criteria are satisfied except for that on $\sum p_{\mathrm{T}}^{b\text{-jet}}/\sum p_{\mathrm{T}}^{\mathrm{jet}}$. The vertical black lines and the corresponding arrows indicate the corresponding cuts defining those regions. All uncertainties are considered. The last bin includes overflow. The 'Other' category contains the rare top, triboson, and other diboson processes with the SS final state. The bottom panel shows the ratio of the observed data to the predicted yields.

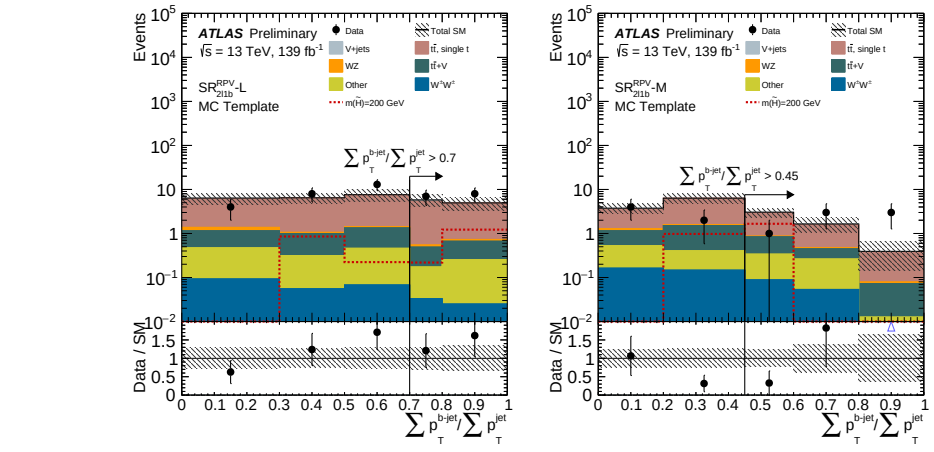

(a) $\mathrm{SR}^{\mathrm{RPV}}_{2\ell 1b}$-L

(b) $\mathrm{SR}^{\mathrm{RPV}}_{2\ell 1b}$-M

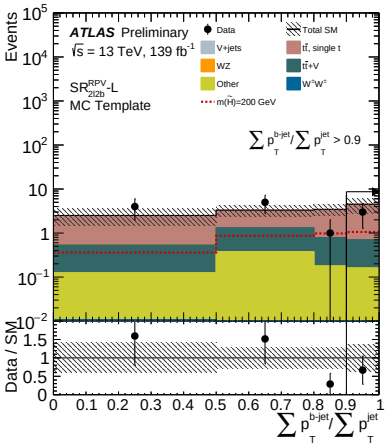

(c) $\mathrm{SR}^{\mathrm{RPV}}_{2\ell 2b}$-L

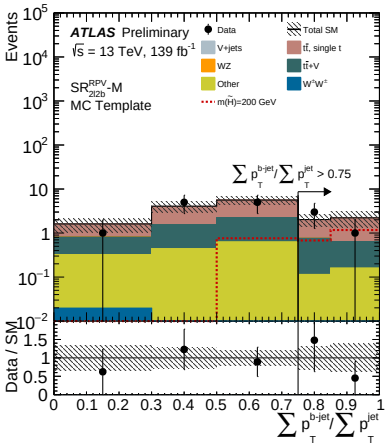

(d) $\mathrm{SR}^{\mathrm{RPV}}_{2\ell 2b}$-M

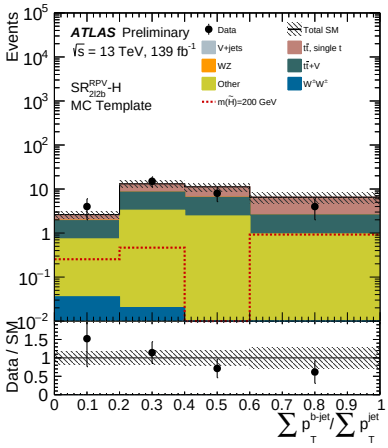

(e) $\mathrm{SR}^{\mathrm{RPV}}_{2\ell 2b}$-H

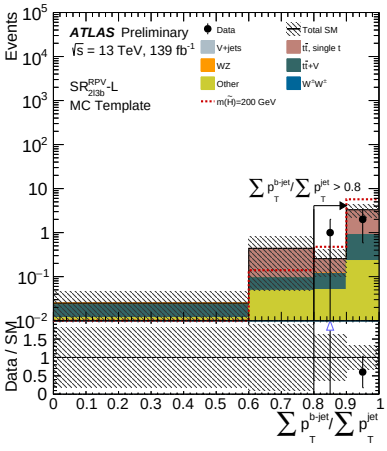

(f) $\mathrm{SR}^{\mathrm{RPV}}_{2\ell 3b}$-L

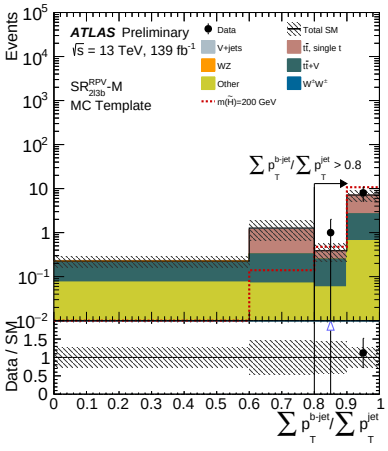

(g) $\mathrm{SR}^{\mathrm{RPV}}_{2\ell 3b}$-M

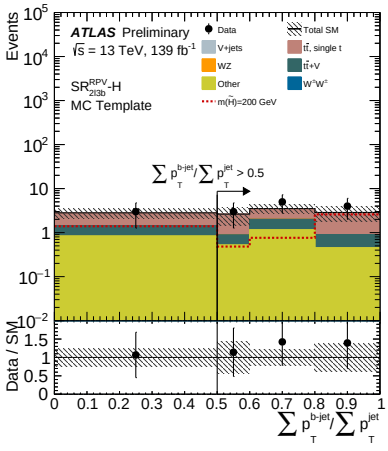

(h) $\mathrm{SR}^{\mathrm{RPV}}_{2\ell 3b}$-H

Figure 23: $\sum p_{\mathrm{T}}^{b\text{-jet}}/\sum p_{\mathrm{T}}^{\mathrm{jet}}$ distributions of the data and the expected background for all SRs defined for the *UDD* RPV model with MC template method applied. All SR selection criteria are satisfied except for that on $\sum p_{\mathrm{T}}^{b\text{-jet}}/\sum p_{\mathrm{T}}^{\mathrm{jet}}$. The vertical black lines and the corresponding arrows indicate the corresponding cuts defining those regions. All uncertainties are considered. The last bin includes overflow. The 'Other' category contains the rare top, triboson, and other diboson processes with the SS final state. The bottom panel shows the ratio of the observed data to the predicted yields.

References

[1] J. Alwall et al., *The automated computation of tree-level and next-to-leading order differential cross sections, and their matching to parton shower simulations*, JHEP **07** (2014) 079, arXiv: 1405.0301 [hep-ph].

[2] P. A. Zyla et al., *Review of Particle Physics*, PTEP **2020** (2020) 083C01.

[3] R. M. Barnett, J. F. Gunion and H. E. Haber, *Discovering supersymmetry with like-sign dileptons*, Phys. Lett. B **315** (1993) 349, arXiv: hep-ph/9306204.

[4] M. Guchait and D. P. Roy, *Like-sign dilepton signature for gluino production at CERN LHC including top quark and Higgs boson effects*, Phys. Rev. D **52** (1995) 133, arXiv: hep-ph/9412329.

[5] Y. Bai and Z. Han, *Top-antitop and Top-top Resonances in the Dilepton Channel at the CERN LHC*, JHEP **04** (2009) 056, arXiv: 0809.4487 [hep-ph].

[6] E. L. Berger, Q.-H. Cao, C.-R. Chen, C. S. Li and H. Zhang, *Top Quark Forward-Backward Asymmetry and Same-Sign Top Quark Pairs*, Phys. Rev. Lett. **106** (2011) 201801, arXiv: 1101.5625 [hep-ph].

[7] T. Plehn and T. M. P. Tait, *Seeking Sgluons*, J. Phys. G **36** (2009) 075001, arXiv: 0810.3919 [hep-ph].

[8] S. Calvet, B. Fuks, P. Gris and L. Valery, *Searching for sgluons in multitop events at a center-of-mass energy of 8 TeV*, JHEP **04** (2013) 043, arXiv: 1212.3360 [hep-ph].

[9] K. J. F. Gaemers and F. Hoogeveen, *Higgs Production and Decay Into Heavy Flavors With the Gluon Fusion Mechanism*, Phys. Lett. B **146** (1984) 347.

[10] G. C. Branco et al., *Theory and phenomenology of two-Higgs-doublet models*, Phys. Rept. **516** (2012) 1, arXiv: 1106.0034 [hep-ph].

[11] F. M. L. Almeida Jr., Y. do Amaral Coutinho, J. A. Martins Simoes, P. P. Queiroz Filho and C. M. Porto, *Same-sign dileptons as a signature for heavy Majorana neutrinos in hadron hadron collisions*, Phys. Lett. B **400** (1997) 331, arXiv: hep-ph/9703441.

[12] A. Atre, T. Han, S. Pascoli and B. Zhang, *The Search for Heavy Majorana Neutrinos*, JHEP **05** (2009) 030, arXiv: 0901.3589 [hep-ph].

[13] R. Contino and G. Servant, *Discovering the top partners at the LHC using same-sign dilepton final states*, JHEP **06** (2008) 026, arXiv: 0801.1679 [hep-ph].

[14] L. Evans and P. Bryant, *LHC Machine*, JINST **3** (2008) S08001.

[15] ATLAS Collaboration, *The ATLAS Experiment at the CERN Large Hadron Collider*, JINST **3** (2008) S08003.

[16] CMS Collaboration, *The CMS Experiment at the CERN LHC*, JINST **3** (2008) S08004.

[17] Y. Golfand and E. Likhtman, *Extension of the Algebra of Poincare Group Generators and Violation of P Invariance*, JETP Lett. **13** (1971) 323, [Pisma Zh. Eksp. Teor. Fiz. **13** (1971) 452].

[18] D. Volkov and V. Akulov, *Is the neutrino a goldstone particle?*, Phys. Lett. B **46** (1973) 109.

[19] J. Wess and B. Zumino, *Supergauge transformations in four dimensions*, Nucl. Phys. B **70** (1974) 39.

[20] J. Wess and B. Zumino, *Supergauge invariant extension of quantum electrodynamics*, Nucl. Phys. B **78** (1974) 1.

[21] S. Ferrara and B. Zumino, *Supergauge invariant Yang-Mills theories*, Nucl. Phys. B **79** (1974) 413.

[22] A. Salam and J. Strathdee, *Super-symmetry and non-Abelian gauges*, Phys. Lett. B **51** (1974) 353.

[23] S. P. Martin, *A Supersymmetry Primer*, Adv. Ser. Direct. High Energy Phys. **18** (1998) 1, arXiv: hep-ph/9709356.

[24] N. Sakai, *Naturalness in supersymmetric GUTS*, Z. Phys. C **11** (1981) 153.

[25] S. Dimopoulos, S. Raby and F. Wilczek, *Supersymmetry and the scale of unification*, Phys. Rev. D **24** (1981) 1681.

[26] L. E. Ibáñez and G. G. Ross, *Low-energy predictions in supersymmetric grand unified theories*, Phys. Lett. B **105** (1981) 439.

[27] S. Dimopoulos and H. Georgi, *Softly broken supersymmetry and SU(5)*, Nucl. Phys. B **193** (1981) 150.

[28] R. Barbieri and G. Giudice, *Upper bounds on supersymmetric particle masses*, Nucl. Phys. B **306** (1988) 63.

[29] B. de Carlos and J. Casas, *One-loop analysis of the electroweak breaking in supersymmetric models and the fine-tuning problem*, Phys. Lett. B **309** (1993) 320, arXiv: hep-ph/9303291.

[30] H. Goldberg, *Constraint on the Photino Mass from Cosmology*, Phys. Rev. Lett. **50** (1983) 1419, Erratum: Phys. Rev. Lett. **103** (2009) 099905.

[31] J. Ellis, J. Hagelin, D. V. Nanopoulos, K. A. Olive and M. Srednicki, *Supersymmetric relics from the big bang*, Nucl. Phys. B **238** (1984) 453.

[32] G. R. Farrar and P. Fayet, *Phenomenology of the production, decay, and detection of new hadronic states associated with supersymmetry*, Phys. Lett. B **76** (1978) 575.

[33] D. Hooper and T. Plehn, *Supersymmetric dark matter: How light can the LSP be?*, Phys. Lett. B **562** (2003) 18, arXiv: hep-ph/0212226.

[34] H. K. Dreiner, *An Introduction to explicit R-parity violation*, Adv. Ser. Direct. High Energy Phys. **21** (2010) 565, ed. by G. L. Kane, arXiv: hep-ph/9707435.

[35] ATLAS Collaboration, *Search for squarks and gluinos in final states with same-sign leptons and jets using* $139\,fb^{-1}$ *of data collected with the ATLAS detector*, JHEP **06** (2020) 046, arXiv: 1909.08457 [hep-ex].

[36] ATLAS Collaboration, *Search for electroweak production of supersymmetric states in scenarios with compressed mass spectra at* $\sqrt{s} = 13$ *TeV with the ATLAS detector*, Phys. Rev. D **97** (2018) 052010, arXiv: 1712.08119 [hep-ex].

[37] CMS Collaboration, *Search for supersymmetry with a compressed mass spectrum in the vector boson fusion topology with 1-lepton and 0-lepton final states in proton–proton collisions at* $\sqrt{s} = 13$ *TeV*, JHEP **08** (2019) 150, arXiv: 1905.13059 [hep-ex].

[38] ATLAS Collaboration, *Searches for electroweak production of supersymmetric particles with compressed mass spectra in* $\sqrt{s} = 13$ *TeV* pp *collisions with the ATLAS detector*, Phys. Rev. D **101** (2020) 052005, arXiv: 1911.12606 [hep-ex].

[39] ATLAS Collaboration, *Search for supersymmetry at* $\sqrt{s} = 8$ *TeV in final states with jets and two same-sign leptons or three leptons with the ATLAS detector*, JHEP **06** (2014) 035, arXiv: 1404.2500 [hep-ex].

[40] ATLAS Collaboration, *Search for direct pair production of a chargino and a neutralino decaying to the* 125 *GeV Higgs boson in* $\sqrt{s} = 8$ *TeV* pp *collisions with the ATLAS detector*, Eur. Phys. J. C **75** (2015) 208, arXiv: 1501.07110 [hep-ex].

[41] ATLAS Collaboration, *Search for supersymmetry at* $\sqrt{s} = 13$ *TeV in final states with jets and two same-sign leptons or three leptons with the ATLAS detector*, Eur. Phys. J. C **76** (2016) 259, arXiv: 1602.09058 [hep-ex].

[42] ATLAS Collaboration, *Search for supersymmetry in final states with two same-sign or three leptons and jets using* $36 fb^{-1}$ *of* $\sqrt{s} = 13$ *TeV* pp *collision data with the ATLAS detector*, JHEP **09** (2017) 084, arXiv: 1706.03731 [hep-ex], Erratum: JHEP **08** (2019) 121.

[43] ATLAS Collaboration, *Search for chargino and neutralino production in final states with a Higgs boson and missing transverse momentum at* $\sqrt{s} = 13$ *TeV with the ATLAS detector*, Phys. Rev. D **100** (2019) 012006, arXiv: 1812.09432 [hep-ex].

[44] CMS Collaboration, *Search for physics beyond the standard model in events with two leptons of same sign, missing transverse momentum, and jets in proton–proton collisions at* $\sqrt{s} = 13$ *TeV*, Eur. Phys. J. C **77** (2017) 578, arXiv: 1704.07323 [hep-ex].

[45] CMS Collaboration, *Search for physics beyond the standard model in events with jets and two same-sign or at least three charged leptons in proton–proton collisions at* $\sqrt{s} = 13$ *TeV*, Eur. Phys. J. C **80** (2020) 752, arXiv: 2001.10086 [hep-ex].

[46] CMS Collaboration, *Search for electroweak production of charginos and neutralinos in proton–proton collisions at* $\sqrt{s} = 13$ *TeV*, JHEP **04** (2021) 147, arXiv: 2106.14246 [hep-ex].

[47] CMS Collaboration, *Search for resonant production of second-generation sleptons with same-sign dimuon events in proton–proton collisions at* $\sqrt{s} = 13$ *TeV*, Eur. Phys. J. C **79** (2019) 305, arXiv: 1811.09760 [hep-ex].

[48] CMS Collaboration, *Search for anomalous production of events with three or more leptons in* pp *collisions at* $\sqrt{s} = 8$ *TeV*, Phys. Rev. D **90** (2014) 032006, arXiv: 1404.5801 [hep-ex].

[49] ATLAS Collaboration, *Search for direct production of charginos and neutralinos in events with three leptons and missing transverse momentum in* $\sqrt{s} = 8$ *TeV* pp *collisions with the ATLAS detector*, JHEP **04** (2014) 169, arXiv: 1402.7029 [hep-ex].

[50] CMS Collaboration, *Search for Top Squarks in R-Parity-Violating Supersymmetry Using Three or More Leptons and b-Tagged Jets*, Phys. Rev. Lett. **111** (2013) 221801, arXiv: 1306.6643 [hep-ex].

[51] ATLAS Collaboration, *Search for electroweak production of supersymmetric particles in final states with two or three leptons at* $\sqrt{s} = 13$ *TeV with the ATLAS detector*, Eur. Phys. J. C **78** (2018) 995, arXiv: 1803.02762 [hep-ex].

[52] CMS Collaboration, *Search for new phenomena with multiple charged leptons in proton—proton collisions at* $\sqrt{s} = 13$ *TeV*, Eur. Phys. J. C **77** (2017) 635, arXiv: 1701.06940 [hep-ex].

[53] CMS Collaboration, *Search for supersymmetry in events with at least three electrons or muons, jets, and missing transverse momentum in proton–proton collisions at* $\sqrt{s} = 13$ *TeV*, JHEP **02** (2018) 067, arXiv: 1710.09154 [hep-ex].

[54] ATLAS Collaboration, *Search for chargino–neutralino production using recursive jigsaw reconstruction in final states with two or three charged leptons in proton–proton collisions at* $\sqrt{s} = 13$ *TeV with the ATLAS detector*, Phys. Rev. D **98** (2018) 092012, arXiv: 1806.02293 [hep-ex].

[55] ATLAS Collaboration, *Search for chargino–neutralino production with mass splittings near the electroweak scale in three-lepton final states in* $\sqrt{s} = 13$ *TeV pp collisions with the ATLAS detector*, Phys. Rev. D **101** (2020) 072001, arXiv: 1912.08479 [hep-ex].

[56] ATLAS Collaboration, *Search for chargino–neutralino pair production in final states with three leptons and missing transverse momentum in* $\sqrt{s} = 13$ *TeV pp collisions with the ATLAS detector*, Eur. Phys. J. C **81** (2021) 1118, arXiv: 2106.01676 [hep-ex].

[57] ATLAS Collaboration, *Search for trilepton resonances from chargino and neutralino pair production in* $\sqrt{s} = 13$ *TeV pp collisions with the ATLAS detector*, Phys. Rev. D **103** (2020) 112003, arXiv: 2011.10543 [hep-ex].

[58] ATLAS Collaboration, *Search for charginos and neutralinos in final states with two boosted hadronically decaying bosons and missing transverse momentum in pp collisions at* $\sqrt{s} = 13$ *TeV with the ATLAS detector*, Phys. Rev. D **104** (2021) 112010, arXiv: 2108.07586 [hep-ex].

[59] ATLAS Collaboration, *Search for direct production of electroweakinos in final states with missing transverse momentum and a Higgs boson decaying into photons in pp collisions at* $\sqrt{s} = 13$ *TeV with the ATLAS detector*, JHEP **10** (2020) 005, arXiv: 2004.10894 [hep-ex].

[60] CMS Collaboration, *Search for electroweak production of charginos and neutralinos in multilepton final states in proton–proton collisions at* $\sqrt{s} = 13$ *TeV*, JHEP **03** (2018) 166, arXiv: 1709.05406 [hep-ex].

[61] V. A. Mitsou, *R-parity violating supersymmetry and neutrino physics: experimental signatures*, PoS **PLANCK2015** (2015) 085, ed. by I. Antoniadis, G. K. Leontaris and K. Tamvakis, arXiv: 1510.02660 [hep-ph].

[62] A. H. Chamseddine, R. L. Arnowitt and P. Nath, *Locally Supersymmetric Grand Unification*, Phys. Rev. Lett. **49** (1982) 970.

[63] R. Barbieri, S. Ferrara and C. A. Savoy, *Gauge Models with Spontaneously Broken Local Supersymmetry*, Phys. Lett. B **119** (1982) 343.

[64] G. L. Kane, C. F. Kolda, L. Roszkowski and J. D. Wells, *Study of constrained minimal supersymmetry*, Phys. Rev. D **49** (1994) 6173, arXiv: hep-ph/9312272.

[65] ATLAS Collaboration, *Search for supersymmetry in final states with jets, missing transverse momentum and one isolated lepton in* $\sqrt{s} = 7$ *TeV pp collisions using* $1\,fb^{-1}$ *of ATLAS data*, Phys. Rev. D **85** (2012) 012006, arXiv: 1109.6606 [hep-ex].

[66] ATLAS Collaboration, *Search for squarks and gluinos in events with isolated leptons, jets and missing transverse momentum at* $\sqrt{s} = 8$ *TeV with the ATLAS detector*, JHEP **04** (2015) 116, arXiv: 1501.03555 [hep-ex].

[67] ATLAS Collaboration, *Search for supersymmetry in events with large missing transverse momentum, jets, and at least one tau lepton in* $20\,fb^{-1}$ *of* $\sqrt{s} = 8$ *TeV proton–proton collision data with the ATLAS detector*, JHEP **09** (2014) 103, arXiv: 1407.0603 [hep-ex].

[68] ATLAS Collaboration, *Summary of the searches for squarks and gluinos using* $\sqrt{s} = 8$ *TeV* pp *collisions with the ATLAS experiment at the LHC*, JHEP **10** (2015) 054, arXiv: 1507.05525 [hep-ex].

[69] ATLAS Collaboration, *Constraints on promptly decaying supersymmetric particles with lepton-number- and R-parity-violating interactions using Run-1 ATLAS data*, ATLAS-CONF-2015-018, 2015, URL: https://cds.cern.ch/record/2017303.

[70] A. Djouadi et al., *The Minimal supersymmetric standard model: Group summary report*, 1998, arXiv: hep-ph/9901246.

[71] C. F. Berger, J. S. Gainer, J. L. Hewett and T. G. Rizzo, *Supersymmetry Without Prejudice*, JHEP **02** (2009) 023, arXiv: 0812.0980 [hep-ph].

[72] ATLAS Collaboration, *Search for massive supersymmetric particles decaying to many jets using the ATLAS detector in* pp *collisions at* $\sqrt{s} = 8$ *TeV*, Phys. Rev. D **91** (2015) 112016, arXiv: 1502.05686 [hep-ex], Erratum: Phys. Rev. D **93** (2016) 039901.

[73] ATLAS Collaboration, *A search for top squarks with R-parity-violating decays to all-hadronic final states with the ATLAS detector in* $\sqrt{s} = 8$ *TeV proton–proton collisions*, JHEP **06** (2016) 067, arXiv: 1601.07453 [hep-ex].

[74] ATLAS Collaboration, *Search for new phenomena in a lepton plus high jet multiplicity final state with the ATLAS experiment using* $\sqrt{s} = 13$ *TeV proton–proton collision data*, JHEP **09** (2017) 088, arXiv: 1704.08493 [hep-ex].

[75] ATLAS Collaboration, *A search for pair-produced resonances in four-jet final states at* $\sqrt{s} = 13$ *TeV with the ATLAS detector*, Eur. Phys. J. C **78** (2018) 250, arXiv: 1710.07171 [hep-ex].

[76] ATLAS Collaboration, *Search for R-parity-violating supersymmetric particles in multi-jet final states produced in* pp *collisions at* $\sqrt{s} = 13$ *TeV using the ATLAS detector at the LHC*, Phys. Lett. B **785** (2018) 136, arXiv: 1804.03568 [hep-ex].

[77] ATLAS Collaboration, *Search for phenomena beyond the Standard Model in events with large b-jet multiplicity using the ATLAS detector at the LHC*, Eur. Phys. J. C **81** (2021) 11, arXiv: 2010.01015 [hep-ex].

[78] CMS Collaboration, *Search for anomalous production of multilepton events in* pp *collisions at* $\sqrt{s} = 7$ *TeV*, JHEP **06** (2012) 169, arXiv: 1204.5341 [hep-ex].

[79] CMS Collaboration, *Searches for R-parity-violating supersymmetry in* pp *collisions at* $\sqrt{s} = 8$ *TeV in final states with 0–4 leptons*, Phys. Rev. D **94** (2016) 112009, arXiv: 1606.08076 [hep-ex].

[80] CMS Collaboration, *Search for R-parity violating supersymmetry with displaced vertices in proton–proton collisions at* $\sqrt{s} = 8$ *TeV*, Phys. Rev. D **95** (2017) 012009, arXiv: 1610.05133 [hep-ex].

[81] CMS Collaboration, *Search for R-parity violating supersymmetry in pp collisions at $\sqrt{s}$ = 13 TeV using b jets in a final state with a single lepton, many jets, and high sum of large-radius jet masses*, Phys. Lett. B **783** (2018) 114, arXiv: 1712.08920 [hep-ex].

[82] CMS Collaboration, *Search for top squarks in final states with two top quarks and several light-flavor jets in proton–proton collisions at $\sqrt{s}$ = 13 TeV*, Phys. Rev. D **104** (2021) 032006, arXiv: 2102.06976 [hep-ex].

[83] ATLAS Collaboration, *Search for R-parity-violating supersymmetry in a final state containing leptons and many jets with the ATLAS experiment using $\sqrt{s}$ = 13 TeV proton–proton collision data*, Eur. Phys. J. C **81** (2021) 1023, arXiv: 2106.09609 [hep-ex].

[84] ATLAS Collaboration, *Reinterpretation of searches for supersymmetry in models with variable R-parity-violating coupling strength and long-lived R-hadrons*, ATLAS-CONF-2018-003, 2018, URL: https://cds.cern.ch/record/2308391.

[85] J. Alwall, M.-P. Le, M. Lisanti and J. G. Wacker, *Searching for directly decaying gluinos at the Tevatron*, Phys. Lett. B **666** (2008) 34, arXiv: 0803.0019 [hep-ph].

[86] J. Alwall, P. Schuster and N. Toro, *Simplified models for a first characterization of new physics at the LHC*, Phys. Rev. D **79** (2009) 075020, arXiv: 0810.3921 [hep-ph].

[87] D. Alves et al., *Simplified models for LHC new physics searches*, J. Phys. G **39** (2012) 105005, arXiv: 1105.2838 [hep-ph].

[88] W. Porod, M. Hirsch, J. Romao and J. W. F. Valle, *Testing neutrino mixing at future collider experiments*, Phys. Rev. D **63** (2001) 115004, arXiv: hep-ph/0011248.

[89] S. Roy and B. Mukhopadhyaya, *Some implications of a supersymmetric model with R-parity breaking bilinear interactions*, Phys. Rev. D **55** (1997) 7020, arXiv: hep-ph/9612447.

[90] J. C. Romao, M. A. Diaz, M. Hirsch, W. Porod and J. W. F. Valle, *A Supersymmetric solution to the solar and atmospheric neutrino problems*, Phys. Rev. D **61** (2000) 071703, arXiv: hep-ph/9907499.

[91] M. Hirsch, M. A. Diaz, W. Porod, J. C. Romao and J. W. F. Valle, *Neutrino masses and mixings from supersymmetry with bilinear R parity violation: A Theory for solar and atmospheric neutrino oscillations*, Phys. Rev. D **62** (2000) 113008, [Erratum: Phys.Rev.D 65, 119901 (2002)], arXiv: hep-ph/0004115.

[92] M. A. Diaz, M. Hirsch, W. Porod, J. C. Romao and J. W. F. Valle, *Solar neutrino masses and mixing from bilinear R parity broken supersymmetry: Analytical versus numerical results*, Phys. Rev. D **68** (2003) 013009, [Erratum: Phys.Rev.D 71, 059904 (2005)], arXiv: hep-ph/0302021.

[93] S. Biswas, E. J. Chun and P. Sharma, *Di-Higgs signatures from R-parity violating supersymmetry as the origin of neutrino mass*, JHEP **12** (2016) 062, arXiv: 1604.02821 [hep-ph].

[94] F. Thomas and W. Porod, *Determining R-parity violating parameters from neutrino and LHC data*, JHEP **10** (2011) 089, arXiv: 1106.4658 [hep-ph].

[95] R. Barbier et al., *R-parity violating supersymmetry*, Phys. Rept. **420** (2005) 1, arXiv: hep-ph/0406039.

[96] C. Csaki, Y. Grossman and B. Heidenreich, *MFV SUSY: A Natural Theory for R-Parity Violation*, Phys. Rev. D **85** (2012) 095009, arXiv: 1111.1239 [hep-ph].

[97] H. Georgi and S. L. Glashow, *Unity of All Elementary Particle Forces*, Phys. Rev. Lett. **32** (1974) 438.

[98] J. D. Bekenstein, *Nonexistence of baryon number for static black holes*, Phys. Rev. D **5** (1972) 1239.

[99] A. D. Sakharov, *Violation of CP Invariance, C asymmetry, and baryon asymmetry of the universe*, Pisma Zh. Eksp. Teor. Fiz. **5** (1967) 32.

[100] ATLAS Collaboration, *ATLAS Insertable B-Layer: Technical Design Report*, ATLAS-TDR-19; CERN-LHCC-2010-013, 2010, URL: https://cds.cern.ch/record/1291633, Addendum: ATLAS-TDR-19-ADD-1; CERN-LHCC-2012-009, 2012, URL: https://cds.cern.ch/record/1451888.

[101] B. Abbott et al., *Production and integration of the ATLAS Insertable B-Layer*, JINST **13** (2018) T05008, arXiv: 1803.00844 [physics.ins-det].

[102] ATLAS Collaboration, *The ATLAS Collaboration Software and Firmware*, ATL-SOFT-PUB-2021-001, 2021, URL: https://cds.cern.ch/record/2767187.

[103] ATLAS Collaboration, *ATLAS data quality operations and performance for 2015–2018 data-taking*, JINST **15** (2020) P04003, arXiv: 1911.04632 [physics.ins-det].

[104] ATLAS Collaboration, *Luminosity determination in pp collisions at $\sqrt{s} = 13$ TeV using the ATLAS detector at the LHC*, ATLAS-CONF-2019-021, 2019, URL: https://cds.cern.ch/record/2677054.

[105] G. Avoni et al., *The new LUCID-2 detector for luminosity measurement and monitoring in ATLAS*, JINST **13** (2018) P07017.

[106] ATLAS Collaboration, *Performance of the ATLAS trigger system in 2015*, Eur. Phys. J. C **77** (2017) 317, arXiv: 1611.09661 [hep-ex].

[107] ATLAS Collaboration, *Performance of electron and photon triggers in ATLAS during LHC Run 2*, Eur. Phys. J. C **80** (2020) 47, arXiv: 1909.00761 [hep-ex].

[108] ATLAS Collaboration, *Performance of the ATLAS muon triggers in Run 2*, JINST **15** (2020) P09015, arXiv: 2004.13447 [hep-ex].

[109] ATLAS Collaboration, *Performance of the missing transverse momentum triggers for the ATLAS detector during Run-2 data taking*, JHEP **08** (2020) 080, arXiv: 2005.09554 [hep-ex].

[110] T. Sjöstrand, S. Mrenna and P. Skands, *A brief introduction to PYTHIA 8.1*, Comput. Phys. Commun. **178** (2008) 852, arXiv: 0710.3820 [hep-ph].

[111] T. Sjöstrand et al., *An introduction to PYTHIA 8.2*, Comput. Phys. Commun. **191** (2015) 159, arXiv: 1410.3012 [hep-ph].

[112] R. D. Ball et al., *Parton distributions with LHC data*, Nucl. Phys. B **867** (2013) 244, arXiv: 1207.1303 [hep-ph].

[113] ATLAS Collaboration, *The Pythia 8 A3 tune description of ATLAS minimum bias and inelastic measurements incorporating the Donnachie–Landshoff diffractive model*, ATL-PHYS-PUB-2016-017, 2016, URL: https://cds.cern.ch/record/2206965.

[114] D. J. Lange, *The EvtGen particle decay simulation package*, Nucl. Instrum. Meth. A **462** (2001) 152.

[115] ATLAS Collaboration, *The ATLAS Simulation Infrastructure*, Eur. Phys. J. C **70** (2010) 823, arXiv: 1005.4568 [physics.ins-det].

[116] GEANT4 Collaboration, S. Agostinelli et al., *GEANT4 – a simulation toolkit*, Nucl. Instrum. Meth. A **506** (2003) 250.

[117] ATLAS Collaboration, *The simulation principle and performance of the ATLAS fast calorimeter simulation FastCaloSim*, ATL-PHYS-PUB-2010-013, 2010, URL: https://cds.cern.ch/record/1300517.

[118] R. Frederix and S. Frixione, *Merging meets matching in MC@NLO*, JHEP **12** (2012) 061, arXiv: 1209.6215 [hep-ph].

[119] ATLAS Collaboration, *ATLAS Pythia 8 tunes to 7 TeV data*, ATL-PHYS-PUB-2014-021, 2014, URL: https://cds.cern.ch/record/1966419.

[120] S. Mrenna and P. Skands, *Automated parton-shower variations in PYTHIA 8*, Phys. Rev. D **94** (2016) 074005, arXiv: 1605.08352 [hep-ph].

[121] L. Lönnblad, *Correcting the Colour-Dipole Cascade Model with Fixed Order Matrix Elements*, JHEP **05** (2002) 046, arXiv: hep-ph/0112284.

[122] L. Lönnblad and S. Prestel, *Matching tree-level matrix elements with interleaved showers*, JHEP **03** (2012) 019, arXiv: 1109.4829 [hep-ph].

[123] W. Porod, *SPheno, a program for calculating supersymmetric spectra, SUSY particle decays and SUSY particle production at e+ e- colliders*, Comput. Phys. Commun. **153** (2003) 275, arXiv: hep-ph/0301101.

[124] W. Porod and F. Staub, *SPheno 3.1: Extensions including flavour, CP-phases and models beyond the MSSM*, Comput. Phys. Commun. **183** (2012) 2458, arXiv: 1104.1573 [hep-ph].

[125] F. Staub, *Exploring new models in all detail with SARAH*, Adv. High Energy Phys. **2015** (2015) 840780, arXiv: 1503.04200 [hep-ph].

[126] A. Vicente, *Computer tools in particle physics*, (2015), arXiv: 1507.06349 [hep-ph].

[127] W. Beenakker et al., *Production of Charginos, Neutralinos, and Sleptons at Hadron Colliders*, Phys. Rev. Lett. **83** (1999) 3780, arXiv: hep-ph/9906298, Erratum: Phys. Rev. Lett. **100** (2008) 029901.

[128] J. Debove, B. Fuks and M. Klasen, *Threshold resummation for gaugino pair production at hadron colliders*, Nucl. Phys. B **842** (2011) 51, arXiv: 1005.2909 [hep-ph].

[129] B. Fuks, M. Klasen, D. R. Lamprea and M. Rothering, *Gaugino production in proton-proton collisions at a center-of-mass energy of 8 TeV*, JHEP **10** (2012) 081, arXiv: 1207.2159 [hep-ph].

[130] B. Fuks, M. Klasen, D. R. Lamprea and M. Rothering,
Precision predictions for electroweak superpartner production at hadron colliders with RESUMMINO,
Eur. Phys. J. C **73** (2013) 2480, arXiv: 1304.0790 [hep-ph].

[131] J. Fiaschi and M. Klasen, *Neutralino-chargino pair production at NLO+NLL with resummation-improved parton density functions for LHC Run II*, Phys. Rev. D **98** (2018) 055014, arXiv: 1805.11322 [hep-ph].

[132] C. Borschensky et al.,
Squark and gluino production cross sections in pp collisions at $\sqrt{s} = 13, 14, 33$ *and* 100 *TeV*,
Eur. Phys. J. C **74** (2014) 3174, arXiv: 1407.5066 [hep-ph].

[133] J. Butterworth et al., *PDF4LHC recommendations for LHC Run II*, J. Phys. G **43** (2016) 023001, arXiv: 1510.03865 [hep-ph].

[134] E. Bothmann et al., *Event generation with Sherpa 2.2*, SciPost Phys. **7** (2019) 034, arXiv: 1905.09127 [hep-ph].

[135] T. Gleisberg and S. Höche, *Comix, a new matrix element generator*, JHEP **12** (2008) 039, arXiv: 0808.3674 [hep-ph].

[136] S. Schumann and F. Krauss,
A parton shower algorithm based on Catani–Seymour dipole factorisation, JHEP **03** (2008) 038, arXiv: 0709.1027 [hep-ph].

[137] S. Höche, F. Krauss, M. Schönherr and F. Siegert,
A critical appraisal of NLO+PS matching methods, JHEP **09** (2012) 049, arXiv: 1111.1220 [hep-ph].

[138] S. Höche, F. Krauss, M. Schönherr and F. Siegert,
QCD matrix elements + parton showers. The NLO case, JHEP **04** (2013) 027, arXiv: 1207.5030 [hep-ph].

[139] S. Catani, F. Krauss, B. R. Webber and R. Kuhn, *QCD Matrix Elements + Parton Showers*, JHEP **11** (2001) 063, arXiv: hep-ph/0109231.

[140] S. Höche, F. Krauss, S. Schumann and F. Siegert, *QCD matrix elements and truncated showers*, JHEP **05** (2009) 053, arXiv: 0903.1219 [hep-ph].

[141] F. Buccioni et al., *OpenLoops 2*, Eur. Phys. J. C **79** (2019) 866, arXiv: 1907.13071 [hep-ph].

[142] F. Cascioli, P. Maierhöfer and S. Pozzorini, *Scattering Amplitudes with Open Loops*, Phys. Rev. Lett. **108** (2012) 111601, arXiv: 1111.5206 [hep-ph].

[143] A. Denner, S. Dittmaier and L. Hofer,
COLLIER: A fortran-based complex one-loop library in extended regularizations,
Comput. Phys. Commun. **212** (2017) 220, arXiv: 1604.06792 [hep-ph].

[144] R. D. Ball et al., *Parton distributions for the LHC run II*, JHEP **04** (2015) 040, arXiv: 1410.8849 [hep-ph].

[145] S. Frixione, G. Ridolfi and P. Nason,
A positive-weight next-to-leading-order Monte Carlo for heavy flavour hadroproduction,
JHEP **09** (2007) 126, arXiv: 0707.3088 [hep-ph].

[146] P. Nason, *A new method for combining NLO QCD with shower Monte Carlo algorithms*, JHEP **11** (2004) 040, arXiv: hep-ph/0409146.

[147] S. Frixione, P. Nason and C. Oleari,
Matching NLO QCD computations with parton shower simulations: the POWHEG method,
JHEP **11** (2007) 070, arXiv: 0709.2092 [hep-ph].

[148] S. Alioli, P. Nason, C. Oleari and E. Re, *A general framework for implementing NLO calculations in shower Monte Carlo programs: the POWHEG BOX*, JHEP **06** (2010) 043,
arXiv: 1002.2581 [hep-ph].

[149] H. B. Hartanto, B. Jäger, L. Reina and D. Wackeroth,
Higgs boson production in association with top quarks in the POWHEG BOX,
Phys. Rev. D **91** (2015) 094003, arXiv: 1501.04498 [hep-ph].

[150] R. Frederix, D. Pagani and M. Zaro, *Large NLO corrections in $t\bar{t}W^{\pm}$ and $t\bar{t}t\bar{t}$ hadroproduction from supposedly subleading EW contributions*, JHEP **02** (2018) 031,
arXiv: 1711.02116 [hep-ph].

[151] S. Frixione, E. Laenen, P. Motylinski and B. R. Webber, *Angular correlations of lepton pairs from vector boson and top quark decays in Monte Carlo simulations*, JHEP **04** (2007) 081,
arXiv: hep-ph/0702198.

[152] P. Artoisenet, R. Frederix, O. Mattelaer and R. Rietkerk,
Automatic spin-entangled decays of heavy resonances in Monte Carlo simulations,
JHEP **03** (2013) 015, arXiv: 1212.3460 [hep-ph].

[153] P. Nason and C. Oleari,
NLO Higgs boson production via vector-boson fusion matched with shower in POWHEG,
JHEP **02** (2010) 037, arXiv: 0911.5299 [hep-ph].

[154] ATLAS Collaboration, *Measurement of the Z/γ^* boson transverse momentum distribution in pp collisions at $\sqrt{s} = 7$ TeV with the ATLAS detector*, JHEP **09** (2014) 145,
arXiv: 1406.3660 [hep-ex].

[155] M. L. Ciccolini, S. Dittmaier and M. Krämer,
Electroweak radiative corrections to associated WH and ZH production at hadron colliders,
Phys. Rev. D **68** (2003) 073003, arXiv: hep-ph/0306234 [hep-ph].

[156] O. Brein, A. Djouadi and R. Harlander,
NNLO QCD corrections to the Higgs-strahlung processes at hadron colliders,
Phys. Lett. B **579** (2004) 149, arXiv: hep-ph/0307206.

[157] O. Brein, R. Harlander, M. Wiesemann and T. Zirke,
Top-quark mediated effects in hadronic Higgs-Strahlung, Eur. Phys. J. C **72** (2012) 1868,
arXiv: 1111.0761 [hep-ph].

[158] L. Altenkamp, S. Dittmaier, R. V. Harlander, H. Rzehak and T. J. E. Zirke,
Gluon-induced Higgs-strahlung at next-to-leading order QCD, JHEP **02** (2013) 078,
arXiv: 1211.5015 [hep-ph].

[159] A. Denner, S. Dittmaier, S. Kallweit and A. Mück, *HAWK 2.0: A Monte Carlo program for Higgs production in vector-boson fusion and Higgs strahlung at hadron colliders*,
Comput. Phys. Commun. **195** (2015) 161, arXiv: 1412.5390 [hep-ph].

[160] O. Brein, R. V. Harlander and T. J. E. Zirke, *vh@nnlo – Higgs Strahlung at hadron colliders*,
Comput. Phys. Commun. **184** (2013) 998, arXiv: 1210.5347 [hep-ph].

[161] R. V. Harlander, A. Kulesza, V. Theeuwes and T. Zirke,
Soft gluon resummation for gluon-induced Higgs Strahlung, JHEP **11** (2014) 082,
arXiv: 1410.0217 [hep-ph].

[162] M. Ciccolini, A. Denner and S. Dittmaier, *Strong and Electroweak Corrections to the Production of a Higgs Boson + 2 Jets via Weak Interactions at the Large Hadron Collider*,
Phys. Rev. Lett. **99** (2007) 161803, arXiv: 0707.0381 [hep-ph].

[163] M. Ciccolini, A. Denner and S. Dittmaier,
Electroweak and QCD corrections to Higgs production via vector-boson fusion at the CERN LHC,
Phys. Rev. D **77** (2008) 013002, arXiv: 0710.4749 [hep-ph].

[164] P. Bolzoni, F. Maltoni, S.-O. Moch and M. Zaro,
Higgs Boson Production via Vector-Boson Fusion at Next-to-Next-to-Leading Order in QCD,
Phys. Rev. Lett. **105** (2010) 011801, arXiv: 1003.4451 [hep-ph].

[165] A. Djouadi, J. Kalinowski and M. Spira, *HDECAY: A program for Higgs boson decays in the Standard Model and its supersymmetric extension*, Comput. Phys. Commun. **108** (1998) 56,
arXiv: hep-ph/9704448.

[166] M. Spira, *QCD Effects in Higgs Physics*, Fortsch. Phys. **46** (1998) 203, arXiv: hep-ph/9705337.

[167] A. Djouadi, M. M. Mühlleitner and M. Spira,
Decays of Supersymmetric particles: The Program SUSY-HIT (SUspect-SdecaY-Hdecay-InTerface),
Acta Phys. Polon. B **38** (2007) 635, arXiv: hep-ph/0609292.

[168] A. Bredenstein, A. Denner, S. Dittmaier and M. M. Weber, *Radiative corrections to the semileptonic and hadronic Higgs-boson decays $H \to WW/ZZ \to 4$ fermions*,
JHEP **02** (2007) 080, arXiv: hep-ph/0611234.

[169] A. Bredenstein, A. Denner, S. Dittmaier and M. M. Weber,
Precise predictions for the Higgs-boson decay $H \to WW/ZZ \to 4$ leptons,
Phys. Rev. D **74** (2006) 013004, arXiv: hep-ph/0604011 [hep-ph].

[170] A. Bredenstein, A. Denner, S. Dittmaier and M. M. Weber,
Precision calculations for the Higgs decays $H \to ZZ/WW \to 4$ leptons,
Nucl. Phys. Proc. Suppl. **160** (2006) 131, arXiv: hep-ph/0607060 [hep-ph].

[171] C. Anastasiou, L. Dixon, K. Melnikov and F. Petriello, *High-precision QCD at hadron colliders: Electroweak gauge boson rapidity distributions at next-to-next-to leading order*,
Phys. Rev. D **69** (2004) 094008, arXiv: hep-ph/0312266.

[172] A. Buckley et al., *A comparative study of Higgs boson production from vector-boson fusion*,
JHEP **11** (2021) 108, arXiv: 2105.11399 [hep-ph].

[173] ATLAS Collaboration, *Studies on top-quark Monte Carlo modelling for Top2016*,
ATL-PHYS-PUB-2016-020, 2016, URL: https://cds.cern.ch/record/2216168.

[174] S. Alioli, P. Nason, C. Oleari and E. Re,
NLO single-top production matched with shower in POWHEG: s- and t-channel contributions,
JHEP **09** (2009) 111, arXiv: 0907.4076 [hep-ph], Erratum: JHEP **02** (2010) 011.

[175] R. Frederix, E. Re and P. Torrielli,
Single-top t-channel hadroproduction in the four-flavour scheme with POWHEG and aMC@NLO,
JHEP **09** (2012) 130, arXiv: 1207.5391 [hep-ph].

[176] S. Frixione, E. Laenen, P. Motylinski, C. White and B. R. Webber, *Single-top hadroproduction in association with a W boson*, JHEP **07** (2008) 029, arXiv: 0805.3067 [hep-ph].

[177] ATLAS Collaboration, *Electron and photon performance measurements with the ATLAS detector using the 2015–2017 LHC proton–proton collision data*, JINST **14** (2019) P12006, arXiv: 1908.00005 [hep-ex].

[178] ATLAS Collaboration, *Muon reconstruction performance of the ATLAS detector in proton–proton collision data at* $\sqrt{s} = 13$ *TeV*, Eur. Phys. J. C **76** (2016) 292, arXiv: 1603.05598 [hep-ex].

[179] ATLAS Collaboration, *Muon reconstruction and identification efficiency in ATLAS using the full Run 2 pp collision data set at* $\sqrt{s} = 13$ *TeV*, Eur. Phys. J. C **81** (2021) 578, arXiv: 2012.00578 [hep-ex].

[180] M. Cacciari, G. P. Salam and G. Soyez, *The anti-*k_t *jet clustering algorithm*, JHEP **04** (2008) 063, arXiv: 0802.1189 [hep-ph].

[181] ATLAS Collaboration, *Jet energy scale measurements and their systematic uncertainties in proton–proton collisions at* $\sqrt{s} = 13$ *TeV with the ATLAS detector*, Phys. Rev. D **96** (2017) 072002, arXiv: 1703.09665 [hep-ex].

[182] ATLAS Collaboration, *Performance of pile-up mitigation techniques for jets in pp collisions at* $\sqrt{s} = 8$ *TeV using the ATLAS detector*, Eur. Phys. J. C **76** (2016) 581, arXiv: 1510.03823 [hep-ex].

[183] ATLAS Collaboration, *ATLAS b-jet identification performance and efficiency measurement with* $t\bar{t}$ *events in pp collisions at* $\sqrt{s} = 13$ *TeV*, Eur. Phys. J. C **79** (2019) 970, arXiv: 1907.05120 [hep-ex].

[184] ATLAS Collaboration, *Optimisation and performance studies of the ATLAS b-tagging algorithms for the 2017-18 LHC run*, ATL-PHYS-PUB-2017-013, 2017, URL: https://cds.cern.ch/record/2273281.

[185] ATLAS Collaboration, *Performance of missing transverse momentum reconstruction with the ATLAS detector using proton–proton collisions at* $\sqrt{s} = 13$ *TeV*, Eur. Phys. J. C **78** (2018) 903, arXiv: 1802.08168 [hep-ex].

[186] ATLAS Collaboration, E_T^{miss} *performance in the ATLAS detector using 2015–2016 LHC pp collisions*, ATLAS-CONF-2018-023, 2018, URL: https://cds.cern.ch/record/2625233.

[187] ATLAS Collaboration, *Selection of jets produced in* 13 *TeV proton–proton collisions with the ATLAS detector*, ATLAS-CONF-2015-029, 2015, URL: https://cds.cern.ch/record/2037702.

[188] ATLAS Collaboration, *Object-based missing transverse momentum significance in the ATLAS Detector*, ATLAS-CONF-2018-038, 2018, URL: https://cds.cern.ch/record/2630948.

[189] G. Cowan, K. Cranmer, E. Gross and O. Vitells, *Asymptotic formulae for likelihood-based tests of new physics*, Eur. Phys. J. C **71** (2011) 1554, arXiv: 1007.1727 [physics.data-an], Erratum: Eur. Phys. J. C **73** (2013) 2501.

[190] M. Baak et al., *HistFitter software framework for statistical data analysis*, Eur. Phys. J. C **75** (2015) 153, arXiv: 1410.1280 [hep-ex].

[191] R. D. Cousins, J. T. Linnemann and J. Tucker,
Evaluation of three methods for calculating statistical significance when incorporating a systematic uncertainty into a test of the background-only hypothesis for a Poisson process,
Nucl. Instrum. Meth. A **595** (2008) 480, arXiv: physics/0702156 [physics.data-an].

[192] ATLAS Collaboration, *Measurement of the WW cross section in $\sqrt{s} = 7$ TeV pp collisions with the ATLAS detector and limits on anomalous gauge couplings*, Phys. Lett. B **712** (2012) 289,
arXiv: 1203.6232 [hep-ex].

[193] ATLAS Collaboration, *Prospects for Higgs boson searches using the $H \to WW^{(*)} \to \ell\nu\ell\nu$ decay mode with the ATLAS detector at* 10 *TeV*, ATL-PHYS-PUB-2010-005, 2010,
URL: https://cds.cern.ch/record/1270568.

[194] ATLAS Collaboration, *Measurement of the top quark-pair production cross section with ATLAS in pp collisions at $\sqrt{s} = 7$ TeV*, Eur. Phys. J. C **71** (2011) 1577, arXiv: 1012.1792 [hep-ex].

[195] ATLAS Collaboration, *Electron reconstruction and identification in the ATLAS experiment using the 2015 and 2016 LHC proton–proton collision data at $\sqrt{s} = 13$ TeV*,
Eur. Phys. J. C **79** (2019) 639, arXiv: 1902.04655 [hep-ex].

[196] ATLAS Collaboration, *Electron and photon energy calibration with the ATLAS detector using 2015–2016 LHC proton–proton collision data*, JINST **14** (2019) P03017,
arXiv: 1812.03848 [hep-ex].

[197] ATLAS Collaboration, *Forward jet vertex tagging using the particle flow algorithm*,
ATL-PHYS-PUB-2019-026, 2019, URL: https://cds.cern.ch/record/2683100.

[198] ATLAS Collaboration, *Jet energy scale and resolution measured in proton–proton collisions at $\sqrt{s} = 13$ TeV with the ATLAS detector*, Eur. Phys. J. C **81** (2020) 689,
arXiv: 2007.02645 [hep-ex].

[199] ATLAS Collaboration, *Measurement of the c-jet mistagging efficiency in $t\bar{t}$ events using pp collision data at $\sqrt{s} = 13$ TeV collected with the ATLAS detector*, Eur. Phys. J. C **82** (2021) 95,
arXiv: 2109.10627 [hep-ex].

[200] ATLAS Collaboration, *Calibration of light-flavour b-jet mistagging rates using ATLAS proton–proton collision data at $\sqrt{s} = 13$ TeV*, ATLAS-CONF-2018-006, 2018,
URL: https://cds.cern.ch/record/2314418.

[201] T. Junk, *Confidence level computation for combining searches with small statistics*,
Nucl. Instrum. Meth. A **434** (1999) 435, arXiv: hep-ex/9902006.

[202] A. L. Read, *Presentation of search results: the CL_S technique*, J. Phys. G **28** (2002) 2693.